CrossMark

J. Fluid Mech. (2018), *vol.* 840, *pp.* 74–105. © Cambridge University Press 2018
doi:10.1017/jfm.2017.905

Three-dimensional doubly diffusive convectons: instability and transition to complex dynamics

Cédric Beaume[1,†], Alain Bergeon[2] and Edgar Knobloch[3]

[1]School of Mathematics, University of Leeds, Leeds LS2 9JT, UK

[2]Institut de Mécanique des Fluides de Toulouse (IMFT), Université de Toulouse, CNRS, 31400 Toulouse, France

[3]Department of Physics, University of California, Berkeley, CA 94720, USA

(Received 1 August 2017; revised 3 November 2017; accepted 12 December 2017; first published online 6 February 2018)

Three-dimensional doubly diffusive convection in a closed vertically extended container driven by competing horizontal temperature and concentration gradients is studied by a combination of direct numerical simulation and linear stability analysis. No-slip boundary conditions are imposed on all six container walls. The buoyancy number N is taken to be -1 to ensure the presence of a conduction state. The primary instability is subcritical and generates two families of spatially localized steady states known as convectons. The convectons bifurcate directly from the conduction state and are organized in a pair of primary branches that snake within a well-defined range of Rayleigh numbers as the convectons grow in length. Secondary instabilities generating twist result in secondary snaking branches of twisted convectons. These destabilize the primary convectons and are responsible for the absence of stable steady states, localized or otherwise, in the subcritical regime. Thus all initial conditions in this regime collapse to the conduction state. As a result, once the Rayleigh number for the primary instability of the conduction state is exceeded, the system exhibits an abrupt transition to large-amplitude relaxation oscillations resembling bursts with no hysteresis. These numerical results are confirmed here by determining the stability properties of both convecton types as well as the domain-filling states. The number of unstable modes of both primary and secondary convectons of different lengths follows a pattern that allows the prediction of their stability properties based on their length alone. The instability of the convectons also results in a dramatic change in the dynamics of the system outside the snaking region that arises when the twist instability operates on a time scale faster than the time scale on which new rolls are nucleated. The results obtained are expected to be applicable in various pattern-forming systems exhibiting localized structures, including convection and shear flows.

Key words: double diffusive convection, instability, nonlinear dynamical systems

1. Introduction

Spatially localized states, both stationary and travelling, are commonly found in fluid flows, notably in convection and shear flows. In this work we are interested in localized states consisting of a segment of a periodic state embedded in a

† Email address for correspondence: c.m.l.beaume@leeds.ac.uk

https://doi.org/10.1017/jfm.2017.905 Published online by Cambridge University Press

homogeneous background state, corresponding either to a conduction state or to laminar shear flow. Much useful and transferable information about states of this type can be gleaned from studies of the bistable Swift–Hohenberg equation in one spatial dimension with periodic boundary conditions and left–right symmetry (Burke & Knobloch 2006). In particular, it is known that in a periodic domain with a finite but large period, localized states bifurcate from the primary branch of subcritical spatially periodic states and that they do so already at small amplitude, i.e. close to the primary bifurcation. This bifurcation is likewise subcritical and in the simplest case generates a pair of unstable localized states with reflection symmetry. However, with decreasing forcing these states acquire stability via folds and thereafter the two branches of localized states oscillate between a pair of well-defined limits in parameter space in a behaviour known as homoclinic snaking (Woods & Champneys 1999). During each back and forth oscillation the localized state grows in length via the nucleation of a new wavelength on either side. As one follows the branches upward each gains stability at a left fold and loses stability at a right fold, thereby generating a large multiplicity of simultaneously stable localized states of different lengths within the snaking region. The wavelength of the structure embedded in the background homogeneous state depends on the location in the snaking region and increases along the stable branch segments from left to right. Close to the folds of the snaking branches, additional bifurcations occur that produce asymmetric spatially localized states. These states, known as rung states, are always unstable and lie on branches that interconnect the intertwined branches of symmetric localized states forming a snakes-and-ladders structure (Burke & Knobloch 2006, 2007*a*,*b*). Related behaviour is present in systems with midplane reflection symmetry (Burke & Knobloch 2007*b*) and in structures localized in two spatial dimensions (Avitabile *et al.* 2010).

Spatially localized states are also found in a large variety of other fluid systems, ranging from ferrofluids (Lloyd *et al.* 2015) to colloidal suspensions (Lioubashevski *et al.* 1999), and display strikingly similar properties. Historically, localized states in fluids were first identified in doubly diffusive convection, a term describing convection in a binary fluid mixture driven by imposed temperature and concentration differences. The first such states, now referred to as convectons, were computed in 1997 in natural doubly diffusive convection in a two-dimensional vertically extended cavity, i.e. convection driven by horizontal gradients (Ghorayeb & Mojtabi 1997) but their snaking structure was discovered only a decade later (Bergeon & Knobloch 2008*b*). Parallel studies of localized doubly diffusive convection in two-dimensional horizontally extended domains (Batiste *et al.* 2006; Mercader *et al.* 2009; Beaume, Bergeon & Knobloch 2011; Mercader *et al.* 2011; Watanabe, Iima & Nishiura 2012, 2016) have established a solid relationship between these types of problems and the phenomenology captured so effectively by the bistable Swift–Hohenberg equation. In shear flows localized states also snake (Schneider, Gibson & Burke 2010*a*; Gibson & Schneider 2016) and moreover may lie on the separatrix between laminar and turbulent flows (Duguet, Schlatter & Henningson 2009; Schneider, Marinc & Eckhardt 2010*b*) and so play a prominent role in the transition to turbulence. An ever-increasing catalogue of localized states in shear flow is now available (Avila *et al.* 2013; Khapko *et al.* 2013; Brand & Gibson 2014; Gibson & Brand 2014; Mellibovsky & Meseguer 2015).

The bistable Swift–Hohenberg equation leads one to expect that below the snaking region localized solutions will collapse towards the conduction state while above the snaking region such solutions will grow in length dynamically, resulting in

https://doi.org/10.1017/jfm.2017.905 Published online by Cambridge University Press

the invasion of the background conduction state by stable convection. This is in fact the case in both two-dimensional natural doubly diffusive convection (Bergeon & Knobloch 2008*b*) and in two-dimensional binary fluid convection in a horizontal layer (Batiste *et al.* 2006). However, this attractive picture of the dynamics does not necessarily extend to three dimensions. Already in 2002 Bergeon and Knobloch showed that in three-dimensional slot convection the large-amplitude domain-filling state is unstable (Bergeon & Knobloch 2002). As a result a subcritical steady state primary instability does not generate a hysteretic transition to large-amplitude stationary convection but results instead in a non-hysteretic transition to a finite-amplitude relaxation oscillation. This remarkable behaviour extends to three-dimensional natural doubly diffusive convection in vertically extended domains (Beaume, Bergeon & Knobloch 2013*a*). In particular, an analogous instability, now responsible for the presence of unstable twisted convectons, destabilizes the quasi-two-dimensional convectons resembling those computed by Bergeon & Knobloch (2008*b*). The consequences of this instability are similar and dramatic: the large-amplitude stationary domain-filling state is destabilized, and convectons both within and above the snaking region collapse to the conduction state instead of evolving to a large-amplitude state (Beaume *et al.* 2013*a*).

This unexpected behaviour motivates the present work. Specifically, we wish to confirm the results of earlier direct numerical simulations of three-dimensional natural doubly diffusive convection by performing explicit linear stability calculations for both the quasi-two-dimensional convectons computed by Bergeon & Knobloch (2008*b*) and the fully three-dimensional twisted convectons computed by Beaume *et al.* (2013*a*). In fact, only Watanabe *et al.* (2016) have thus far investigated the detailed stability properties of localized states in a fluid flow, and this in the context of two-dimensional binary fluid convection in a horizontal layer with a negative Soret effect. The present work extends this type of analysis to three dimensions and provides an exhaustive account of the stability properties of convectons in three-dimensional natural doubly diffusive convection. The results confirm those obtained in direct numerical simulations and provide a guide to understanding the complex dynamics displayed by the present system near threshold for the primary instability of the conduction state.

In the following section, we introduce the specific case of natural doubly diffusive convection that we study and summarize the state of the art. Section 3 provides an exhaustive account of the stability properties of each of the various convecton types known to be present in this system and describes the results of direct numerical simulations of the system in the vicinity of the snaking region. The paper concludes with a summary and discussion of the results obtained.

2. Problem set-up

2.1. *Doubly diffusive convection*

Following Beaume *et al.* (2013*a*) we consider doubly diffusive convection in a binary fluid placed within a three-dimensional box of square cross-section in the horizontal and large extent in the vertical. We use the coordinate x for the vertical direction and (y, z) for the horizontal coordinates. Convection is produced by competing but balanced horizontal gradients of temperature and concentration that result from the imposition of appropriate Dirichlet boundary conditions at $z = 0, l$ leading to the conduction state $\boldsymbol{u}^* = 0$, $T^* = T_r + z\Delta T/l$, $C^* = C_r + z\Delta C/l$, where $\boldsymbol{u}^*$ is the velocity, T^* is the temperature, C^* is the concentration of the heavier component of the binary mixture (hereafter shortened to concentration), T_r and C_r are reference temperature and concentration and $\Delta T > 0$ and $\Delta C > 0$ are the imposed temperature

https://doi.org/10.1017/jfm.2017.905 Published online by Cambridge University Press

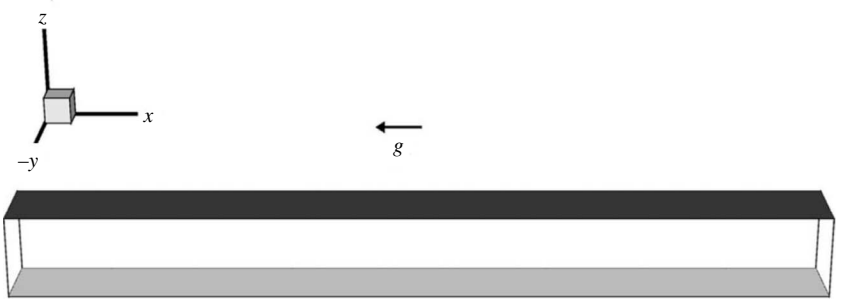


FIGURE 1. Sketch of the physical domain from an angle similar to that used in subsequent figures. For convenience the system has been rotated anticlockwise by 90° around the y axis, i.e. clockwise on the page. As a result, the acceleration due to gravity points towards the left. Shaded boundaries are maintained at fixed temperature and concentration with the darker wall maintained at higher values of T and C than the lighter one. Only a portion of the domain in x is shown.

and concentration differences across the box. We non-dimensionalize the governing equations using l for lengths, ΔT for the temperature, ΔC for the concentration and l^2/κ for the time, where κ is the thermal diffusivity. In the absence of cross-diffusion, the Boussinesq equations describing the system are

$$Pr^{-1}\left[\partial_t \boldsymbol{u} + (\boldsymbol{u}\cdot\boldsymbol{\nabla})\,\boldsymbol{u}\right] = -\boldsymbol{\nabla} p + Ra(T-C)\hat{\boldsymbol{x}} + \nabla^2\boldsymbol{u}, \tag{2.1}$$

$$\boldsymbol{\nabla}\cdot\boldsymbol{u} = 0, \tag{2.2}$$

$$\partial_t T + (\boldsymbol{u}\cdot\boldsymbol{\nabla})\,T = \nabla^2 T, \tag{2.3}$$

$$\partial_t C + (\boldsymbol{u}\cdot\boldsymbol{\nabla})\,C = \tau\nabla^2 C. \tag{2.4}$$

Here $\boldsymbol{u} = (u, v, w)$ is the dimensionless velocity field in (x, y, z) coordinates, p is the dimensionless pressure, $T \equiv (T^* - T_r)/\Delta T$ is the dimensionless temperature and $C \equiv (C^* - C_r)/\Delta C$ is the dimensionless concentration. The above equations involve three dimensionless numbers: the Rayleigh number $Ra \equiv g|\rho_T|\Delta T l^3/\rho_0\nu\kappa$, the Prandtl number $Pr \equiv \nu/\kappa$ and the (inverse) Lewis number $\tau \equiv D/\kappa$, where g is the gravitational acceleration, $\rho_T/\rho_0 < 0$ is the thermal expansion coefficient in the Boussinesq approximation evaluated at T_r, ρ_0 is the density of the fluid at T_r and ν and D are, respectively, the kinematic viscosity and the molecular diffusivity of the heavier fluid component, both assumed to be constant. In writing this set of equations, we have assumed that the buoyancy ratio $N \equiv \rho_C\Delta C/\rho_T\Delta T = -1$, where $\rho_C/\rho_0 > 0$ is the solutal expansion coefficient evaluated at T_r, C_r. With this choice of N the system (2.1)–(2.4) possesses the stationary conduction solution alluded to above.

The physical domain is a closed container of square horizontal cross-section and aspect ratio $L \gg 1$ in the vertical direction, as shown in figure 1. We prescribe no-slip boundary conditions for the velocity everywhere and no-flux boundary conditions for the temperature and concentration on all walls except $z = 0, 1$:

$$x = 0, L \;:\; u = v = w = \partial_x T = \partial_x C = 0, \tag{2.5}$$

$$y = 0, 1 \;:\; u = v = w = \partial_y T = \partial_y C = 0, \tag{2.6}$$

$$z = 0 \;:\; u = v = w = T = C = 0, \tag{2.7}$$

$$z = 1 \;:\; u = v = w = T - 1 = C - 1 = 0. \tag{2.8}$$

https://doi.org/10.1017/jfm.2017.905 Published online by Cambridge University Press

The system (2.1)–(2.4), together with the boundary conditions (2.5)–(2.8), admits the conduction solution $(u, v, w, T, C) = (0, 0, 0, z, z)$ for all values of the parameters Ra, Pr and τ. In terms of the perturbation quantities $(u, v, w, \Theta, \Sigma)$ with $\Theta \equiv T - z$ and $\Sigma \equiv C - z$, the system is equivariant with respect to the dihedral group D_2 generated by the two reflections

$$S_y : [u, v, w, \Theta, \Sigma](x, y, z) \longrightarrow [u, -v, w, \Theta, \Sigma](x, 1 - y, z), \tag{2.9}$$

$$S_\Delta : [u, v, w, \Theta, \Sigma](x, y, z) \longrightarrow [-u, v, -w, -\Theta, -\Sigma](L - x, y, 1 - z). \tag{2.10}$$

The group structure implies that the equations are also equivariant with respect to $S_c = S_y \circ S_\Delta$:

$$S_c : [u, v, w, \Theta, \Sigma](x, y, z) \longrightarrow -[u, v, w, \Theta, \Sigma](L - x, 1 - y, 1 - z). \tag{2.11}$$

These symmetries play a key role in the properties of the solutions described below. In particular, the symmetry S_Δ plays a role that is analogous to the role played by spatial reflection symmetry in the Swift–Hohenberg equation.

When $N \neq -1$ the properties of the system change dramatically. In particular, there is no motionless conduction state and the base state now consists of a single large scale roll that spans the whole domain $0 \leqslant x \leqslant L$. This circulation is responsible for changing the primary bifurcation to an imperfect bifurcation for values of N close to -1. Additional effects can be identified for N farther away from -1. In this paper we focus on the case $N = -1$ only.

We solve the system (2.1)–(2.4) numerically using a splitting scheme for time evolution and a finely tuned numerical continuation algorithm (Beaume 2017). Throughout this paper, the parameters are chosen following Xin, Le Quéré & Tuckerman (1998), Bergeon & Knobloch (2002): $Pr = 1$, $\tau = 1/11$ and $L = 19.8536$, corresponding to eight wavelengths of the primary instability of the two-dimensional problem. The Rayleigh number Ra is kept as a control parameter.

2.2. *State of the art*

Spatially localized solutions of doubly diffusive convection in a vertically extended domain have been studied for over 10 years. Their origin was first investigated in a study of near-onset behaviour in a two-dimensional vertically periodic slot of relatively small spatial period (Bergeon & Knobloch 2008*a*). These authors found a number of spatially periodic states yielding a complex bifurcation diagram and identified states composed of a single roll occupying a part of the domain. This study was followed up by a study describing the evolution of spatially localized doubly diffusive convectons in the same configuration but with a large spatial period in the vertical direction (Bergeon & Knobloch 2008*b*). The authors showed that the primary bifurcation from the conduction state is subcritical. The resulting spatially periodic solution is S_Δ-symmetric and transforms rapidly into an array of corotating rolls as one proceeds away from the primary bifurcation, before turning towards larger values of Ra at a fold and generating an array of large-amplitude corotating rolls. During this process the solution remains S_Δ-symmetric. Subsequent branches of spatially periodic states with different wavenumbers but also S_Δ symmetry behave in the same way but may acquire stability at large amplitude. As expected from earlier studies of the Swift–Hohenberg equation, the primary subcritical branch of spatially periodic states becomes unstable almost immediately to spatially modulated states – still S_Δ-symmetric – and these evolve rapidly with decreasing Ra into strongly localized

https://doi.org/10.1017/jfm.2017.905 Published online by Cambridge University Press

states exhibiting homoclinic snaking (Woods & Champneys 1999; Burke & Knobloch 2006). As in the Swift–Hohenberg equation there are two branches of localized states, one consisting of an odd number of corotating rolls all rotating anticlockwise (clockwise on the page, see figure 1) about the y axis and the other of an even number of corotating rolls also rotating anticlockwise. In the following we refer to these states as L^+ and L^-, respectively, and emphasize that each is S_Δ-symmetric with respect to the centre of the domain. In contrast to the Swift–Hohenberg equation, however, the doubly diffusive problem is not gradient-like and therefore all asymmetric solutions on the rungs of the snakes-and-ladders structure of the bifurcation diagram correspond to states that drift in the x direction. States of this type were not computed in Bergeon & Knobloch (2008*a*,*b*) as they are expected to be unstable, and are likewise not computed here. Such drifting states were computed in related systems, however, confirming the basic bifurcation scenario (Mercader *et al.* 2013; Lo Jacono, Bergeon & Knobloch 2017).

The above properties of the system persist in two-dimensional domains with end walls at $x = 0, L$. However, such walls destroy the translation invariance of the system in the x direction and prevent the formation of spatially periodic solutions (Beaume *et al.* 2013*a*). As a result localized states bifurcate directly from the conduction state (Mercader *et al.* 2009) rather than appearing in a secondary bifurcation from a periodic state. This behaviour persists in three-dimensional domains with no-slip walls (Sezai & Mohamad 2000; Bergeon & Knobloch 2002). In this case all the primary branches have an additional symmetry, the reflection symmetry S_y. This symmetry exerts a substantial influence on the properties of the resulting solutions since it can be broken in secondary bifurcations, a fact responsible for the formation of twisted localized states (Beaume *et al.* 2013*a*), as discussed further below.

The bifurcation diagram for steady doubly diffusive convectons in a three-dimensional domain of square cross-section and aspect ratio $L = 19.8536$ is shown in figure 2. The solutions are represented in terms of the total kinetic energy:

$$E = \frac{1}{2}\int_0^1\int_0^1\int_0^L (u^2 + v^2 + w^2)\,\mathrm{d}x\,\mathrm{d}y\,\mathrm{d}z. \tag{2.12}$$

The figure shows that the convectons bifurcate directly from the conduction state in a transcritical bifurcation at $Ra \approx 850.86$. This bifurcation gives rise to two branches of convectons, L^+ and L^-, both of which snake within the interval $703 \lesssim Ra \lesssim 807$. Both types of convectons are fully symmetric, i.e. invariant under S_y, S_Δ and, by extension, S_c. Convectons from the branch L^+ possess an odd number of corotating, anticlockwise rolls centred in the domain while those from the branch L^- possess an even number of corotating, anticlockwise rolls also centred (see figure 3). These states differ from those found in a two-dimensional periodic domain in minor ways only: (i) because the boundary conditions at $x = 0, L$ are no longer periodic, no spatially periodic state is present and the convectons therefore cannot and do not connect to any spatially periodic state, and (ii) owing to the no-slip boundary condition in y, the convecton structure is fully three-dimensional. Despite these differences, the snaking in the two-dimensional and three-dimensional systems is similar: in the direction of increasing energy, going from a left fold to the next right fold (hereafter called a positive segment, alluding to the fact that Ra increases), the corotating rolls strengthen, while going from a right fold to the next left fold (hereafter called a negative segment: Ra decreases) results in the nucleation of one new roll on either side of the existing roll structure.

https://doi.org/10.1017/jfm.2017.905 Published online by Cambridge University Press

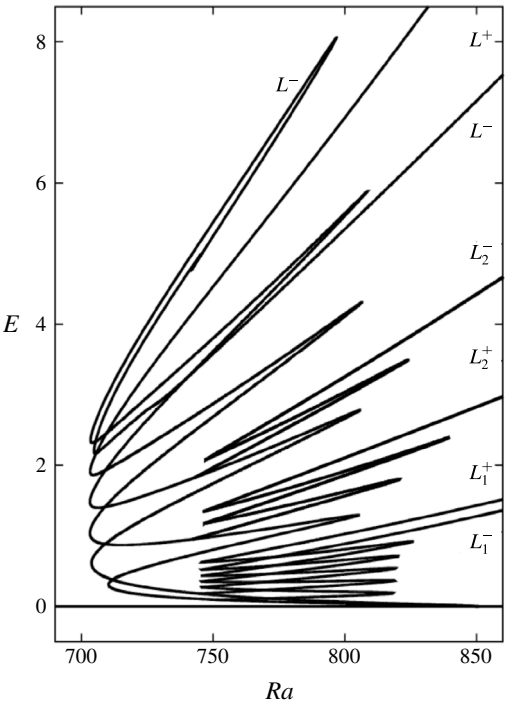


FIGURE 2. Bifurcation diagram representing the total kinetic energy E as a function of the Rayleigh number Ra. The solution $E = 0$ corresponds to the conduction state and convectons ($E > 0$) emerge through a sequence of bifurcations from the conduction state at $Ra \approx 850.86$. The primary branches $L^{\pm}$ consist of corotating rolls with axes parallel to the y axis. Solutions on the secondary branches L^+_1, L^+_2 and L^-_1, L^-_2 bifurcate from $L^{\pm}$ and break the symmetry S_y. Such states are referred to as twisted.

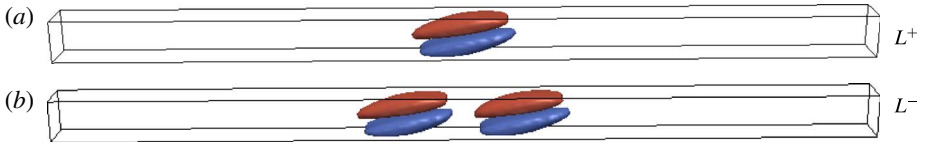


FIGURE 3. (Colour online) Convectons with the lowest kinetic energy along the branch L^+ at $Ra = 710.4464$ (a) and L^- at $Ra = 703.9686$ (b) represented in terms of the isocontours $u = \pm 0.3$. Positive values are shown in red. In this and subsequent figures x points to the right (gravitational acceleration is to the left) and z points upward.

Secondary bifurcations occur along the negative segments of these snaking branches. These symmetry-breaking bifurcations all break the S_y symmetry together with one other reflection and yield roll structures we refer to as twisted. In these states the axes of adjacent rolls are rotated in opposite directions around the vertical axis. One such pitchfork bifurcation occurs along the first negative segment of L^+ (counting from low to high energy) and yields the branch L^+_1 of twisted convectons, while two bifurcations occur in very close succession along the first negative segment of L^-. One of these yields the branch L^-_1 shown in figure 2 but we have not been able to continue the states created in the other. The states on the L^+_1 branch near its birth consist of a

https://doi.org/10.1017/jfm.2017.905 Published online by Cambridge University Press

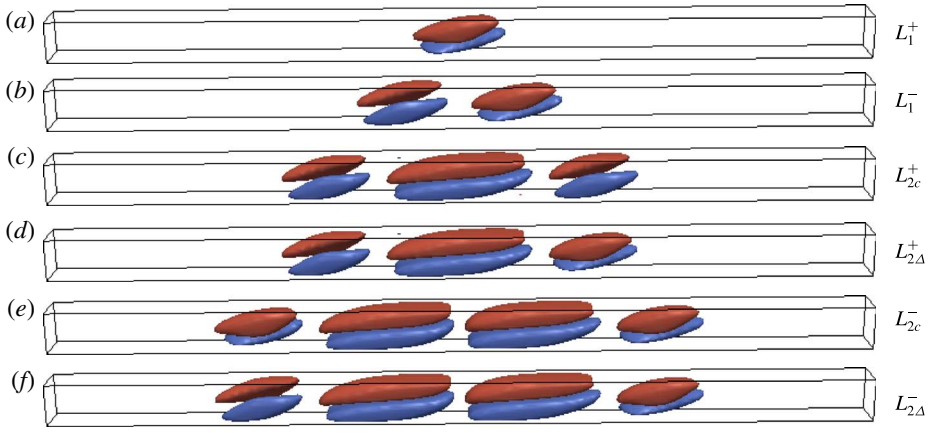


FIGURE 4. (Colour online) Convectons with the lowest kinetic energy along the branch L_1^+ at $Ra = 817.9884$ (a), L_1^- at $Ra = 818.0300$ (b), L_{2c}^+ at $Ra = 820.0688$ (c), $L_{2\Delta}^+$ at $Ra = 820.1873$ (d), L_{2c}^- at $Ra = 823.9576$ (e) and $L_{2\Delta}^-$ at $Ra = 823.4842$ (f) represented in the same way as in figure 3.

single S_c-symmetric roll, i.e. a roll whose axis is rotated about the vertical, while the L_1^- branch consists of two-roll S_Δ-symmetric states rotated in opposite directions about this axis. These states are shown in figure 4(a,b).

Successive secondary bifurcations yielding both S_c- and S_Δ-symmetric twisted convectons can be found along each subsequent negative segment of each primary branch. We refer to the S_c-symmetric states bifurcating from the second negative segment of the L^+ branch as L_{2c}^+ and to the S_Δ-symmetric states bifurcating from this segment as $L_{2\Delta}^+$. These branches are indistinguishable in the bifurcation diagram in figure 2 and are therefore labelled L_2^+ for simplicity. Both consist of solutions composed of one broad untwisted roll inherited from the L^+ branch, surrounded by two narrower rolls of smaller amplitude and rotated about the x axis, as shown in figure 4(c,d). This figure also shows solutions L_{2c}^- and $L_{2\Delta}^-$ produced in successive bifurcations along the second negative segment of L^- (figure 4e,f). These secondary branches produce secondary snaking in $745 \lesssim Ra \lesssim 819$ but the mechanism differs from that responsible for the primary snaking. Going from a left fold to the next right fold in the direction of increasing energy (positive segment), the dominant effect is a rotation of the roll axes about the x axis. Past the right fold, each structure gradually nucleates a pair of new rolls, one on either side, with rotation that is always opposite to that of the roll adjacent to it.

Having recapitulated existing results we now present three examples of the evolution of the system initialized with the three-dimensional states just described. In figure 5(a) we present the temporal evolution of a quasi-two-dimensional localized L^- convecton, followed in figure 5(b) by that of an initial condition taken from the same branch but that is domain-filling and in figure 5(c) by that of a secondary twisted convecton from the L_1^+ branch. The time evolution is represented in terms of the convection amplitude quantified through the quantity

$$A_{conv} = \sqrt{\int_0^1 \int_0^1 u^2 \mathrm{d}y\, \mathrm{d}z}. \tag{2.13}$$

https://doi.org/10.1017/jfm.2017.905 Published online by Cambridge University Press

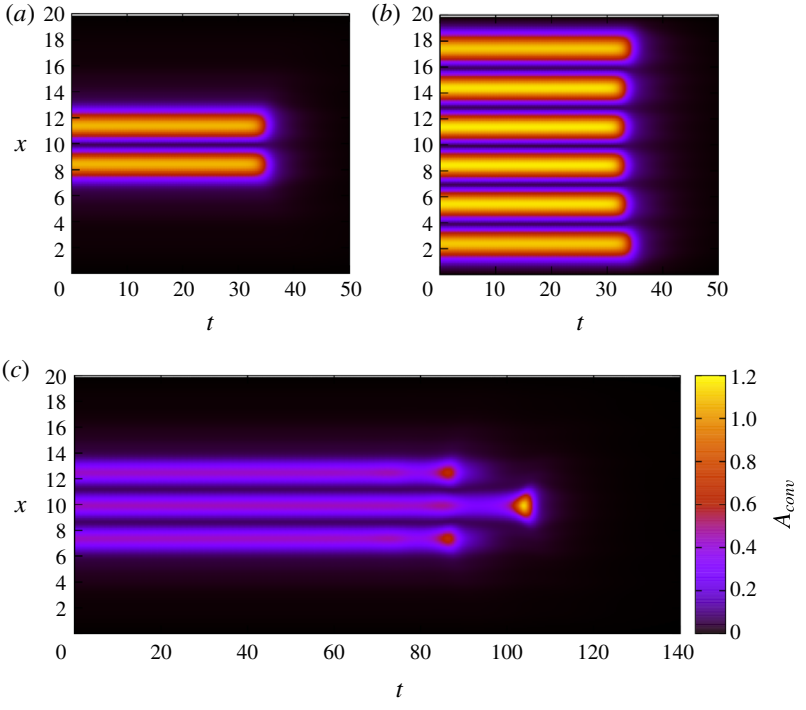


FIGURE 5. (Colour online) Space–time evolution of three subcritical states: (*a*) L^- convecton obtained at $Ra \approx 747.14104$ and time integrated at $Ra = 747.1410$, (*b*) L^- convecton obtained at $Ra \approx 756.04067$ and time integrated at $Ra = 756.0407$ and (*c*) L_1^+ convecton obtained at $Ra \approx 775.76716$ and time integrated at $Ra = 775.7672$.

This measure of convection strength is appropriate since u is the dominant velocity component. The interesting and remarkable fact is that all our initial conditions ultimately collapse to the conduction state, whether they are very localized, domain-filling or twisted. This observation suggests that all the non-trivial states in the subcritical regime of this problem are unstable. The main goal of this paper is to explain this remarkable fact and explore its consequences.

3. Convecton stability

In this section, we report on the stability properties of the primary convectons $L^\pm$ together with those of the twisted convectons $L^\pm_{iS}$, with $i = 1, 2$ and $S = c, \Delta$. Our results describe the evolution of all unstable eigenmodes along the snaking branches and the stability of a given convecton is hereafter reported in terms of a pair of integers (N_r, N_i), where N_r represents the number of real unstable eigenvalues and N_i the number of pairs of unstable complex conjugate ones. Eigenmodes with a real unstable eigenvalue correspond to instabilities with monotonic growth while those with a complex pair of unstable eigenvalues correspond to instabilities with oscillatory growth.

To generate these results, we compute the stability along the snaking branches from Beaume *et al.* (2013*a*) at frequent intervals using the arclength s to step along the

https://doi.org/10.1017/jfm.2017.905 Published online by Cambridge University Press

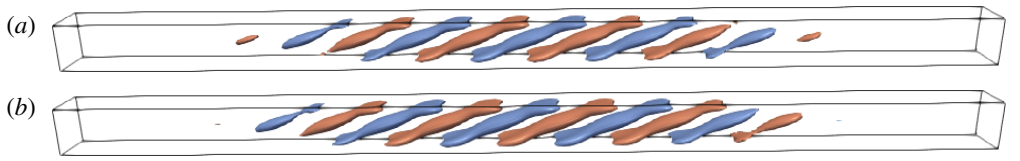


FIGURE 6. (Colour online) (*a*) Odd eigenmode responsible for the pitchfork bifurcation at $Ra \approx 850.78$. (*b*) Even eigenmode responsible for the transcritical bifurcation at $Ra \approx 850.86$. Both eigenmodes are computed at $Ra = 850.8$ and represented using the two isocontours $\tilde{u} = \pm 0.5 \max(|\tilde{u}|)$.

branch. For this purpose we perturb the stationary solutions $\boldsymbol{F}(\boldsymbol{x})$ in the following way:

$$\boldsymbol{f}(\boldsymbol{x}, t) = \boldsymbol{F}(\boldsymbol{x}) + \epsilon \mathrm{Re}\{\tilde{\boldsymbol{f}}(\boldsymbol{x}) e^{\lambda t}\}, \tag{3.1}$$

where ϵ is a small real parameter and $\tilde{\boldsymbol{f}}(\boldsymbol{x})$ is the eigenfunction corresponding to the complex temporal growth rate $\lambda \equiv \lambda_r + i\lambda_i$. We refer to λ_r as the growth rate and λ_i as the frequency of the mode and present the growth rate results in terms of the quantity e^{λ_r}. Eigenvalues λ_r such that $e^{\lambda_r} > 1$ (respectively < 1) are associated with unstable (respectively stable) eigenmodes.

It is important to emphasize here that the bifurcation generating the convectons is in fact the second primary bifurcation (Beaume *et al.* 2013*a*). The first instability takes place at $Ra \approx 850.78$, i.e. slightly earlier than the transcritical bifurcation at $Ra \approx 850.86$. This bifurcation breaks the symmetry S_Δ but respects S_y (the corresponding eigenmode is shown in figure 6*a*) and so is a pitchfork. However, this bifurcation is expected to be subcritical (Bergeon & Knobloch 2002), a fact confirmed here by direct numerical simulations (not shown), and hence does not lead to stable small-amplitude states. However, the presence of this bifurcation is key in one important respect: the resulting weakly unstable eigenvalue is inherited by both convecton branches, and as shown below, plays a significant role in their dynamics. The next mode that becomes unstable is an even mode that breaks no symmetry (figure 6*b*), and the corresponding bifurcation, at $Ra \approx 850.86$, is therefore transcritical. This bifurcation generates the branches $L^\pm$ of spatially localized convectons. Of the pair of branches that result the subcritical branch evolves into the convecton branch L^+ while the supercritical branch evolves into the convecton branch L^-; the latter undergoes a fold at very small amplitude at which it turns towards smaller values of Ra. These small-amplitude results are summarized in figure 7.

The alternation between symmetry-breaking and symmetry-preserving bifurcation is a standard feature of symmetric bifurcation problems (Hirschberg & Knobloch 1997) and is responsible for much of the weakly nonlinear behaviour observed in such systems. Here both modes are spatially modulated, a consequence of the no-slip boundary conditions at the top and bottom of the domain. The linear eigenmodes of the nonlinear states that result likewise split into odd and even families. Specifically, the since both L^+ and L^- are even under appropriate reflections all eigenmodes of $L^\pm$ will have either odd or even parity.

3.1. *Stability of the primary convectons*

Our eigenvalue computations show that all unstable modes of the convecton branches $L^\pm$ are associated with monotonic growth: $\lambda_i = 0$. Figure 8 shows the resulting

https://doi.org/10.1017/jfm.2017.905 Published online by Cambridge University Press

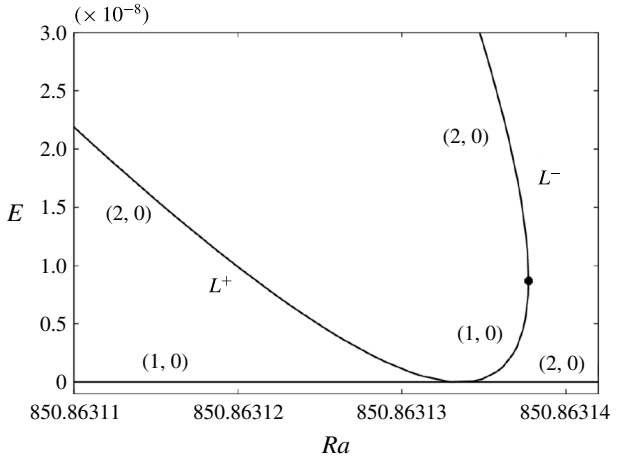


FIGURE 7. Enlargement of the vicinity of the primary transcritical bifurcation at $Ra \approx 850.86$ producing the convecton branches L^+ and L^- in figure 2. Note how close the saddle-node (full circle) on L^- is to the primary bifurcation both in terms of the kinetic energy E and the Rayleigh number Ra. Stability is indicated in terms of the notation (N_r, N_i) introduced in the text.

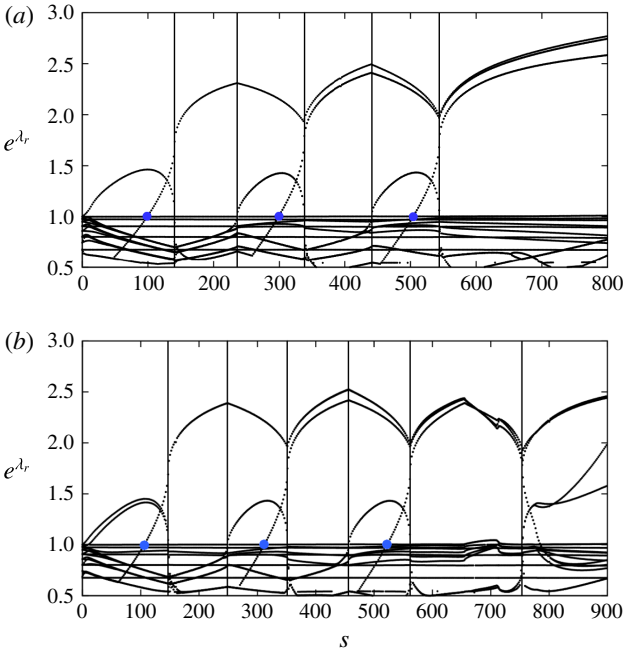


FIGURE 8. (Colour online) Linear stability results for L^+ (*a*) and L^- (*b*). The results are presented in terms of the quantity e^{λ_r} and shown as a function of the arclength s along the branch. Folds correspond to saddle-node bifurcations ($\lambda_r = 0$) and are denoted by vertical lines. Bifurcations generating twist are denoted by a blue dot. One weakly unstable eigenvalue ($e^{\lambda_r} \approx 1$) is always present.

https://doi.org/10.1017/jfm.2017.905 Published online by Cambridge University Press

Until $s \approx$	100	139	236	300	337	443	503	544	800	
L^+ stability	(2,0)	(3,0)	(2,0)	(4,0)	(6,0)	(4,0)	(6,0)	(8,0)	(6,0)	
Until $s \approx$	12	108	148	252	314	351	459	525	561	650
L^- stability	(2,0)	(3,0)	(5,0)	(3,0)	(5,0)	(7,0)	(5,0)	(7,0)	(9,0)	(7,0)

TABLE 1. Stability count associated with the branches L^+ (top two lines) and L^- (bottom two lines) as a function of the arclength s. The first number represents the number of unstable real eigenvalues while the second number shows the number of pairs of unstable complex conjugate of eigenvalues. The count was stopped at $s = 800$ for L^+ and $s \approx 650$ for L^- where the branch undergoes a saddle node induced by the finite size of the domain.

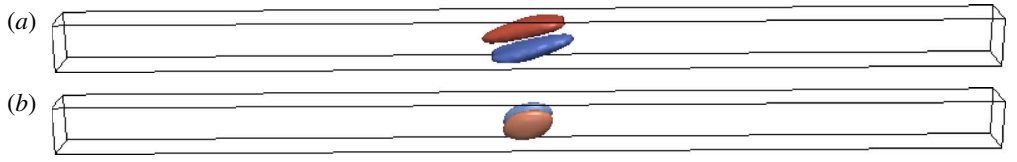


FIGURE 9. (Colour online) (*a*) L^+ convecton at $Ra \approx 749.6782$ ($s \approx 101$) represented using the same colour scheme as in figure 3. (*b*) Twist instability eigenmode for the state in (*a*) represented using the two isocontours $\tilde{u} = \pm 0.5 \max(|\tilde{u}|)$.

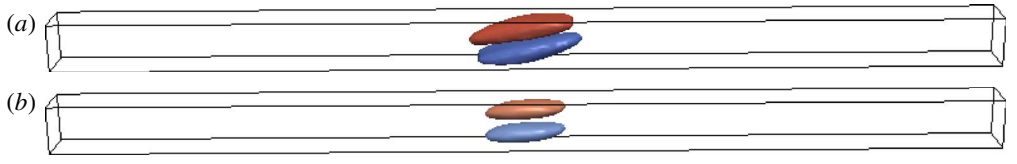


FIGURE 10. (Colour online) (*a*) L^+ convecton at $Ra \approx 711.6782$ ($s \approx 139$) represented using the same colour scheme as in figure 3. (*b*) Amplitude eigenmode for the state in (*a*) represented in the same way as in figure 9(*b*). This eigenmode is responsible for both the primary bifurcation and the first saddle node of L^+.

growth rates λ_r along both branches as a function of the arclength s. The L^+ branch is subcritical and is thus characterized by one unstable amplitude mode in addition to the unstable eigendirection inherited from the primary pitchfork (see table 1). The branch becomes three times unstable at $s \approx 100$ ($Ra \approx 750$) owing to the onset of the twist instability responsible for the secondary branch L_1^+. The twist instability is triggered by the eigenmode shown in figure 9. The eigenmode represents a perturbation roll that is rotated around the x axis by 90° as compared to that in the base state, resulting in the progressive rotation of the convection roll around the x axis as the instability develops. At $s \approx 139$, the branch undergoes a saddle-node bifurcation where the mode shown in figure 10 becomes stable. This mode has a similar profile to that of the base state and is thus an amplitude mode: any instability arising from this mode either strengthens or weakens the base convection roll. This eigenmode remains stable along the whole subsequent snaking branch as it acts only on the central roll. The next two saddle nodes are caused by the destabilization and restabilization of a different eigenmode, shown in figure 11(*b*). The figure shows that this mode is responsible for the addition of one convection roll on either side of the localized structure, a process that takes place just beyond this fold ($s \approx 236$). This eigenmode becomes

https://doi.org/10.1017/jfm.2017.905 Published online by Cambridge University Press

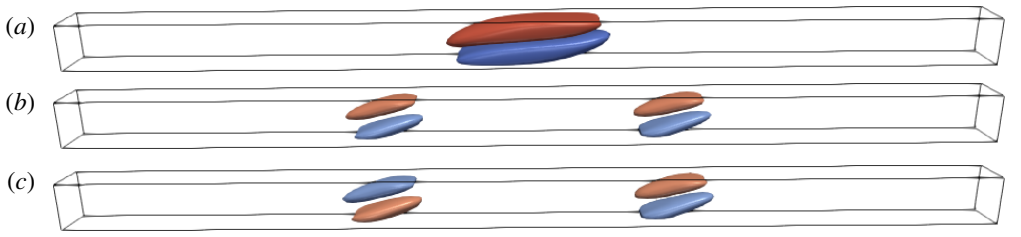


FIGURE 11. (Colour online) (*a*) L^+ convecton at $Ra \approx 802.1785$ ($s \approx 239$) represented using the same colour scheme as in figure 3. (*b*) Amplitude and (*c*) phase eigenmodes for the state in (*a*) represented in the same way as in figure 9(*b*). The former is responsible for the second and third saddle nodes while the latter is responsible for the emergence of drifting rung states via parity-breaking bifurcations.

stabilizing at the next saddle node ($s \approx 337$) and remains so thereafter since it always determines the stability of the same two rolls. Consequently, each subsequent pair of saddle nodes is generated by a new and different eigenmode. This is so for the phase mode (figure 11*c*) as well, and is in contrast to the Swift–Hohenberg equation where the same two amplitude and phase eigenvalues repeatedly pass through zero as one follows the snaking branches (Burke & Knobloch 2006; Kao, Beaume & Knobloch 2014; Knobloch 2015). The saddle node at $s \approx 236$ is followed shortly thereafter by a symmetry-breaking bifurcation triggered by a phase mode, breaking the S_Δ and S_c symmetries but preserving the S_y symmetry. This bifurcation creates a corotating roll on one side of the structure and a counter-rotating roll on the other side. Since $\tau < 1$, the growth of the latter is suppressed by nonlinear terms (Thangam, Zebib & Chen 1982) resulting in the creation of a branch of asymmetric rung states. Owing to the non-gradient nature of the present system this asymmetric state will necessarily drift (in the x direction) until such time as it comes into contact with one of the end walls and comes to rest (see below). The next change in stability is located farther away on the negative segment at $s \approx 300$ ($Ra \approx 740$, see table 1) where two successive bifurcations take place in rapid succession. These bifurcations are of the same nature: they are both produced by eigenmodes breaking the symmetry S_y and one other symmetry, and result in rotation of the axes of the end rolls either in the same or opposite direction as shown in figure 12. Since these modes act on the end rolls, their regions of influence are separated by the central roll where the eigenmode vanishes. As a result, there is little dynamical difference between them and the associated bifurcations occur at similar values of s, equivalently Ra. These twist modes destabilize the solution yet further. However, near the next left saddle node (at $s \approx 335$) the amplitude and phase mode stabilize again, albeit at slightly different values of Ra. This scenario then repeats during each and every oscillation of the L^+ branch. Overall, the L^+ solution gains two unstable eigendirections during each such oscillation, as summarized in table 1.

The branch L^- emerges supercritically from the transcritical bifurcation that produces L^+ but is initially once unstable, owing to the pitchfork bifurcation that precedes it. The branch undergoes a saddle node at low amplitude as shown in figure 7 where the solution gains a second unstable eigendirection and thereafter undergoes a similar sequence of bifurcations as L^+, as summarized in table 1. The eigenvalue count is initialized at the small-amplitude saddle node. At $s \approx 12$ ($Ra \approx 838$), the solution gains a third unstable direction with the corresponding eigenmode shown in

https://doi.org/10.1017/jfm.2017.905 Published online by Cambridge University Press

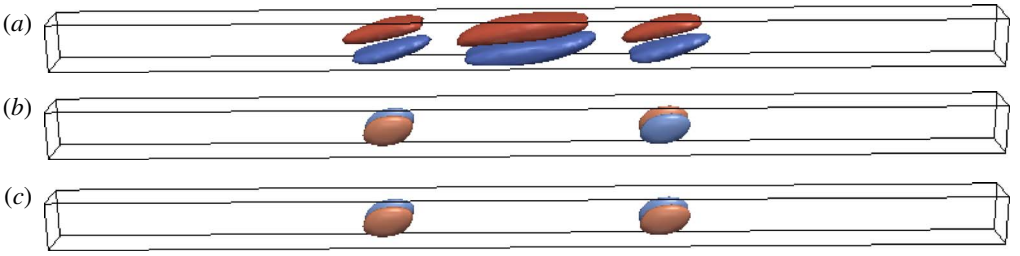


FIGURE 12. (Colour online) (*a*) L^+ convecton at $Ra \approx 738.1785$ ($s \approx 303$) represented using the same colour scheme as in figure 3. (*b*) S_Δ-preserving twist eigenmode for the state in (*a*). (*c*) S_c-preserving twist eigenmode for the state in (*a*). Both eigenmodes are represented in the same way as in figure 9(*b*).

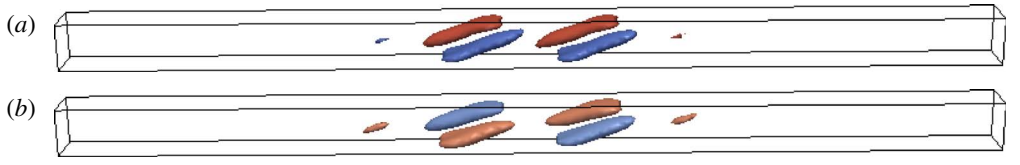


FIGURE 13. (Colour online) (*a*) L^- convecton at $Ra \approx 837.8913$ ($s \approx 12$) represented using the same colour scheme as in figure 3 but for isocontours $u = \pm 0.1$. (*b*) Eigenmode for the state in (*a*) represented in the same way as in figure 9(*b*).

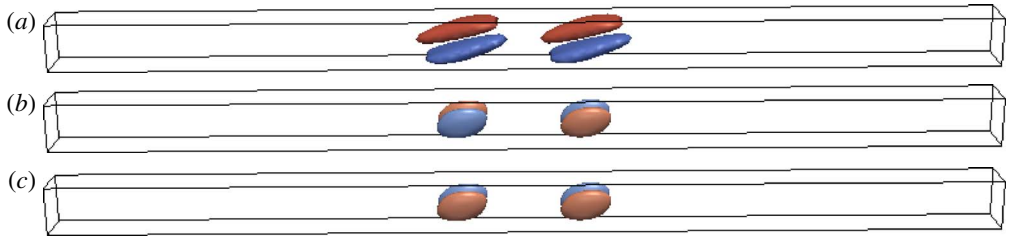


FIGURE 14. (Colour online) (*a*) L^- convecton at $Ra \approx 741.8996$ ($s \approx 108$) represented using the same colour scheme as in figure 3. (*b*) S_Δ-preserving twist eigenmode for the state in (*a*). (*c*) S_c-preserving twist eigenmode for the state in (*a*). Both eigenmodes are represented in the same way as in figure 9(*b*).

figure 13. The figure shows that this mode strengthens one of the end rolls comprising the solution at the expense of the other. This instability likely corresponds to the termination of the branch created in the primary pitchfork bifurcation (Bergeon & Knobloch 2002). Proceeding up the negative branch segment, one next encounters a pair of near-simultaneous bifurcations at $s \approx 108$ ($Ra \approx 742$) responsible for generating the twisted states labelled L_1^- following similar notation for L_1^+ (figure 14). After this original set of bifurcations, the L^- branch follows a similar behaviour to L^+, gaining two unstable eigendirections during each back and forth oscillation of the branch in parameter space: the phase mode stabilizes just below the left fold followed by the amplitude mode before destabilizing in reverse order at the right fold. A pair of twist instabilities occurs along each negative segment of the branch leading to the net generation of two unstable eigendirections per back and forth oscillation.

https://doi.org/10.1017/jfm.2017.905 Published online by Cambridge University Press

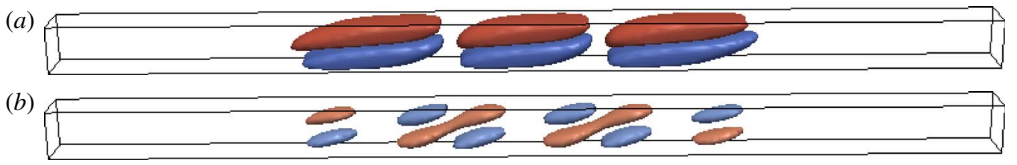


FIGURE 15. (Colour online) (*a*) L^+ convecton at $Ra \approx 805.7820$ ($s \approx 440$) represented using the same colour scheme as in figure 3. (*b*) Odd parity drift eigenmode for the state in (*a*) represented in the same way as in figure 9(*b*).

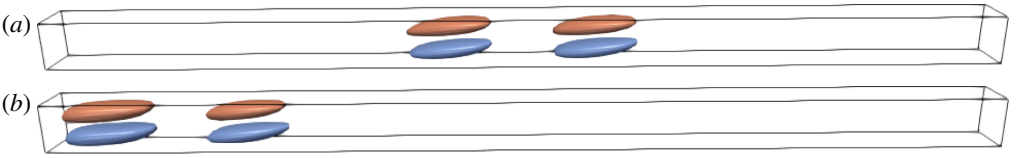


FIGURE 16. (Colour online) Initial condition (*a*) and final state (*b*) obtained through direct numerical simulation with imposed S_y symmetry at $Ra = 757.141$ ($s \approx 200$). The states are represented by the isocontours $|u| = 1.1$.

It will have been observed that both L^+ and L^- possess a weakly unstable eigenvalue, with growth rate around $\lambda_r \approx 10^{-4}$ for a one-roll (strongly localized) state and $\lambda_r \approx 10^{-3}$ for a six-roll (domain-filling) state. The corresponding eigenfunction for a L^+ solution consisting of three convection rolls is shown in figure 15(*b*) and is of odd parity. Here and in the following we use this term to refer to eigenfunctions that are odd with respect to S_Δ, the symmetry of $L^\pm$, but invariant under S_y. In a vertically unbounded system bifurcations triggered by the destabilization of an odd parity mode are associated with the onset of drift and are sometimes called drift bifurcations.

To unveil the consequences of the presence of this mode, we selected a solution that allows us to suppress all other unstable eigendirections by imposing appropriate symmetry conditions on a time simulation. For this purpose we selected a solution on the second positive segment of L^- (counting the very small-amplitude segment shown in figure 7) at $Ra \approx 757.1410$ consisting of a pair of convection rolls. This state is shown in figure 16(*a*) and possesses three unstable eigendirections, two of which are associated with the twist instability and are even in x (see figure 8) and one with odd parity in x. Since the twist instability breaks the symmetry S_y while the odd parity mode does not, we isolate the dynamics of the latter by imposing the symmetry S_y in our time simulation. The effect of the odd parity mode is represented in figure 17 using the quantity A_{conv} defined in expression (2.13). The figure shows that drift occurs on a time scale of the order of 10^4 time units, a time scale that compares well with the magnitude of the odd parity mode eigenvalue. In this simulation, the convecton drifts downward until it meets the bottom wall. By symmetry, an upward drifting convecton can also be obtained. When the convecton meets the wall, it stops drifting and settles into a steady state in which the roll closest to the wall is stronger than that farther away. This wall-attached convecton has been converged using a Newton method (see figure 16*b*) and is twice unstable, each unstable eigendirection being responsible for the twist of one of the rolls. We expect that these states also snake, much like similar states in binary fluid convection in a horizontal layer (Mercader *et al.* 2011).

https://doi.org/10.1017/jfm.2017.905 Published online by Cambridge University Press

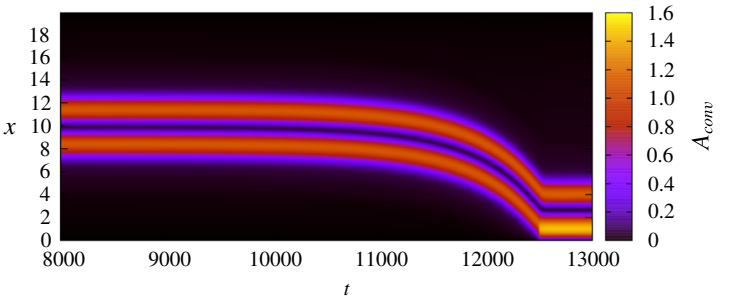


FIGURE 17. (Colour online) Space–time evolution at $Ra = 757.141$ of the quantity A_{conv} defined in expression (2.13) and initialized with the state in figure 16(*a*).

We can understand these results as follows. In an unbounded, translation-invariant system a growing odd parity perturbation would render an even state asymmetric. Since in such systems asymmetric states generically drift, the appearance of such an unstable mode is associated with a parity-breaking or drift bifurcation. In the present case, however, the walls at $x = 0, L$ prevent translation, implying that the presence of a growing odd mode must lead to a stationary state. A simple model equation, studied by Knobloch, Hettel & Dangelmayr (1995) and Dangelmayr, Hettel & Knobloch (1997), captures the effect of broken translation invariance on the parity-breaking bifurcation. The model takes the form

$$\dot{c} = (\mu + \delta\cos\phi - c^2)c + \eta\sin\phi; \quad \dot{\phi} = c - \epsilon\sin\phi, \tag{3.2a,b}$$

where μ is the bifurcation parameter and δ, η, ϵ are parameters proportional to the amplitude of the spatial inhomogeneity, assumed small and of period 2π. When these terms are absent equation (3.2) reduces to the normal form for the parity-breaking bifurcation, assumed here to occur at $\mu = 0$ and to be supercritical, with c the drift speed and ϕ the spatial phase or displacement. When δ, η, ϵ are non-zero c is no longer a drift speed but must be interpreted as the degree of asymmetry of the state. There are then generically two fixed points $(c, \phi) = (0, 0)$ and $(0, \pi)$, corresponding to a symmetric state at the 'wall' ($\phi = 0$) and a symmetric state at the centre of the domain ($\phi = \pi$), respectively. Other, asymmetric fixed points (with $c \neq 0$) may be present as well (Knobloch *et al.* 1995; Dangelmayr *et al.* 1997) but we focus here on the symmetric states. These have opposite stability properties implying that if $(0, 0)$ is stable then $(0, \pi)$ is unstable and vice versa. We identify the symmetry-breaking perturbation of a symmetric convecton at the centre as the perturbation that initially generates translation, but that is arrested by pinning arising from the wall either at $x = 0$ or $x = L$ that brings this state to rest. In our case the final state that results is not symmetric but this is a consequence of the non-periodic boundary conditions employed in the simulation.

3.2. *Stability of the twisted convectons*

The stability properties along the lowest branches of twisted convectons, $L_1^{\pm}$, are summarized in figure 18. The S_c-symmetric twisted convectons on L_1^+ bifurcate towards higher Rayleigh numbers and are thus initially three times unstable: in addition to the unstable eigendirection associated with the twist instability and responsible for the formation of the branch, the L_1^+ convectons are also unstable with respect to an amplitude mode (responsible for the primary transcritical bifurcation)

https://doi.org/10.1017/jfm.2017.905 Published online by Cambridge University Press

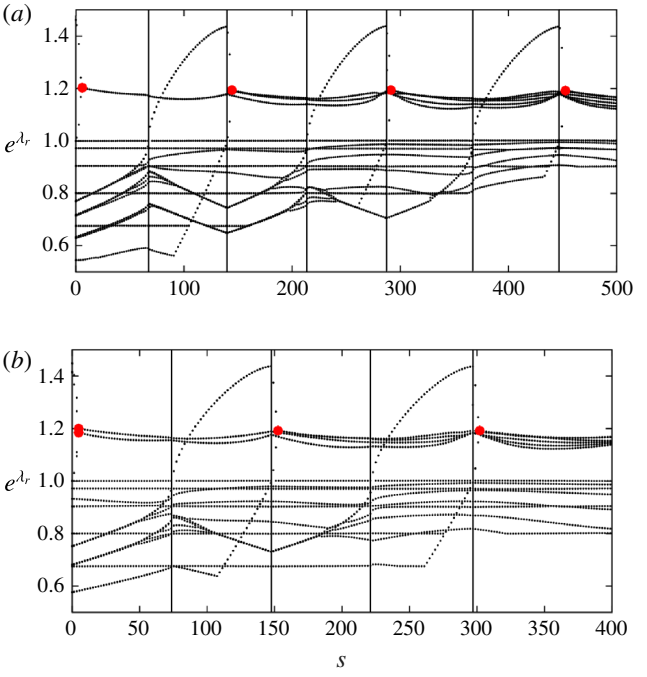


FIGURE 18. (Colour online) Linear stability results for L_1^+ (a) and L_1^- (b). The results are presented in terms of the quantity e^{λ_r} and shown as a function of the arclength s along the branch. Folds correspond to saddle-node bifurcations ($\lambda_r = 0$) and are denoted by vertical lines. Eigenvalue collisions are indicated by a red dot.

and a phase mode inherited from the odd parity drift mode of L^+. Very close to the bifurcation point to L_1^+ the amplitude eigenvalue decreases while the twist eigenvalue increases resulting in an eigenvalue collision at $s \approx 4.7$ ($Ra \approx 756.1$) forming a complex conjugate pair. Such a collision is possible because both modes have the same symmetry and is shown in the left panel of figure 19; the imaginary part of the eigenvalues along the L_1^+ branch is shown in figure 20. The resulting (1, 1) unstable L_1^+ convecton continues to larger values of Ra with the unstable eigenmodes at $Ra \approx 781.9884$ shown in figure 21.

The odd parity drift mode of the twisted convecton shown in figure 21(a) is generally associated with slow dynamics while the observable fast dynamics is generated by unstable oscillatory modes (figure 21b,c) that rotate the convection roll about the x axis first in one direction and then back to its original state. To illustrate this behaviour, we initialized a simulation using an L_1^+ convecton at $Ra \approx 801.9884$ placed in the centre of a larger domain in order to reduce the influence of the walls. This convecton is three times unstable. The simulation is run at $Ra = 801.9884$ and we let the instability grow from numerical error. Selected snapshots from the simulation are shown in figure 22. The snapshots show that the amplitude of the roll first grows to a maximum, its axis then rotates about the x axis before its amplitude and rotation angle decrease again and the process repeats. This process can be seen in the transition from panel (b) at $t = 75$ to (c) at $t = 85$ where the roll straightens and shrinks, before regrowing as in (d) at $t = 95$, and then rotating again as in (e) at $t = 99$ before its ultimate decay to the conduction state.

https://doi.org/10.1017/jfm.2017.905 Published online by Cambridge University Press

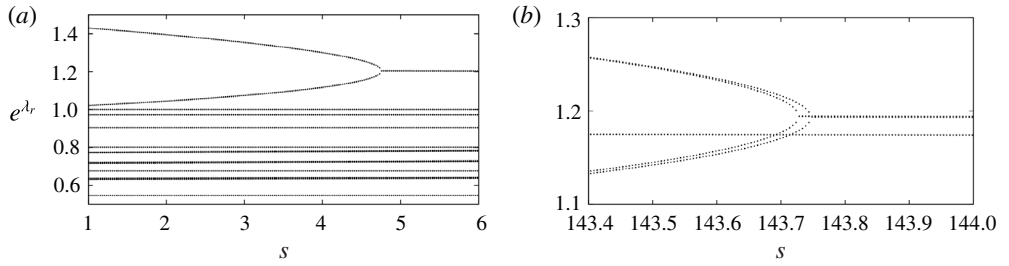


FIGURE 19. Enlargement of the $s \in [1, 6]$ interval (a) and of the $s \in [143.4, 144]$ interval (b) for L_1^+ (figure 18a). One eigenvalue collision occurs at $s \approx 4.7$ while two successive collisions are observed at $s \approx 143.7$. After each of these collisions, the associated eigenvalues become complex conjugate eigenvalues.

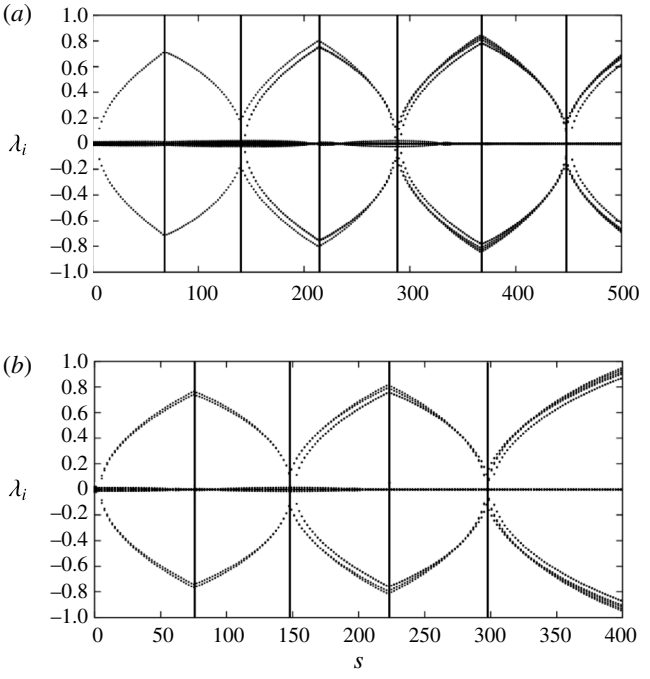


FIGURE 20. Imaginary part of the eigenvalues from the linear stability analysis of L_1^+ (a) and L_1^- (b) as a function of the arclength s along the branch. Saddle nodes are denoted by vertical lines.

In the vicinity of the right fold, the L_1^+ solution gains two more unstable eigendirections in rapid succession: at $Ra \approx 818.29402$, a second mode with a real growth rate and same symmetry as the odd parity drift mode becomes unstable and its eigenvalue collides with that of the odd parity eigenmode to form a complex pair of eigenvalues at $Ra \approx 818.29409$. At this stage and right before the saddle node, the solution stability is thus (0, 2). The saddle-node bifurcation corresponding to the right fold occurs at $Ra \approx 818.29457$ and beyond this point the solution is (1, 2) unstable. By $Ra \approx 818.29446$ the eigenvalues that collided right before the saddle node recombine on the positive real axis and then split, producing a state that is

https://doi.org/10.1017/jfm.2017.905 Published online by Cambridge University Press

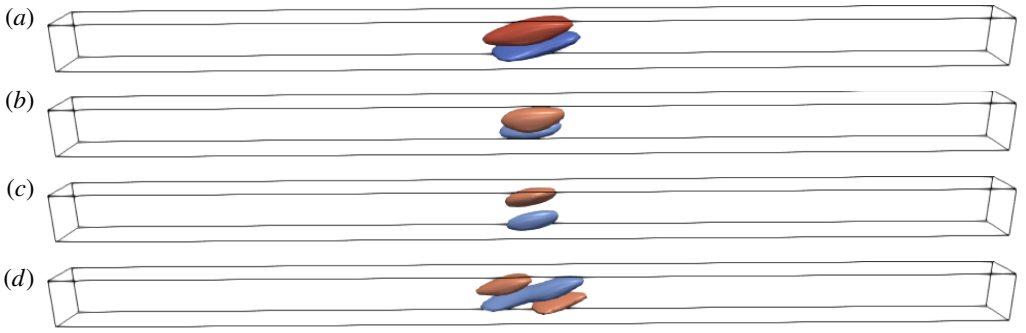


FIGURE 21. (Colour online) (*a*) L_1^+ convecton at $Ra \approx 781.9884$ ($s \approx 31$) represented using the same colour scheme as in figure 3. All unstable eigenmodes are represented as in figure 9(*b*): (*b*, *c*) show the real and imaginary parts of the complex conjugate modes, while (*d*) shows the odd parity drift mode.

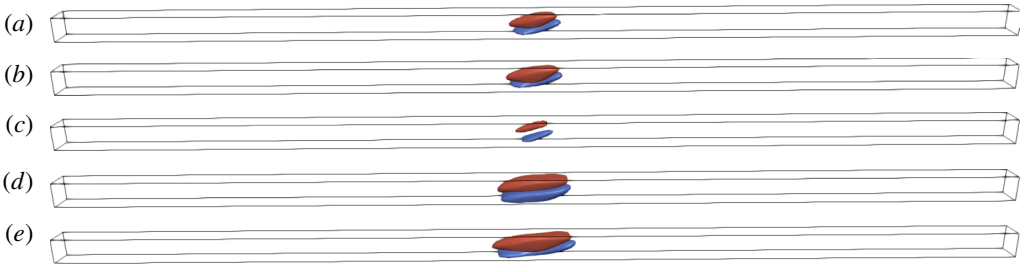


FIGURE 22. (Colour online) (*a*) L_1^+ convecton at $Ra \approx 801.9884$ ($s \approx 51$) used as initial condition for a time simulation in a domain of aspect ratio $2L$. Snapshots of the simulation taken at $t = 76$ (*b*), $t = 85$ (*c*), $t = 95$ (*d*) and $t = 96$ (*e*) span a quasi-period of the oscillations observed. All states are represented using the same colour scheme as in figure 3.

(3, 1) unstable. This behaviour is shown in figure 23. The solution remains (3, 1) unstable until the leftmost fold where the stability again changes in a non-trivial way. This fold occurs at $Ra \approx 745.35871$ where the convecton gains an additional unstable eigendirection. At $Ra \approx 745.35876$, above the fold, a further eigenmode becomes unstable making the solution (5, 1) unstable. The two new unstable modes collide with the two unstable modes inherited from the dynamics close to $s = 143.7$, as shown in the right panel of figure 19, forming two pairs of unstable complex modes and making the solution (1, 3) unstable. This process repeats all along the L_1^+ branch and the solution gains two pairs of unstable complex conjugate eigenvalues after each snaking oscillation.

The stability of the S_Δ-symmetric L_1^- solutions follows the same pattern: after a pair of initial collisions (two collisions occur, see figure 18), the solution is (1, 2) unstable along most of the positive segment of the branch. Like L_1^+ this state acquires an additional unstable mode close to the rightmost saddle node and the associated eigenvalue collides with that of the (unstable) drift eigenmode shortly thereafter to form an additional unstable complex conjugate pair of eigenvalues. Approaching the first fold, the L_1^- solution is (0, 3) unstable. It acquires a new unstable eigendirection at the saddle node and shortly thereafter the most recent complex pair of eigenvalues

https://doi.org/10.1017/jfm.2017.905 Published online by Cambridge University Press

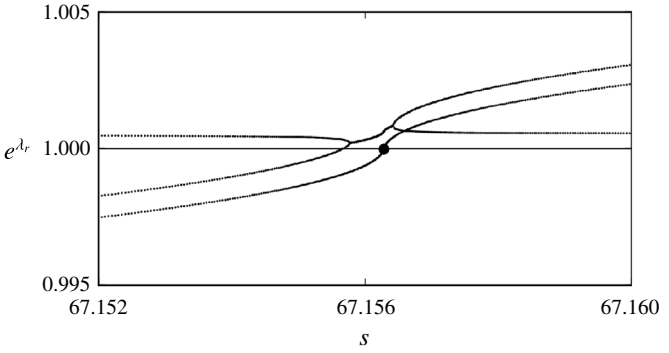


FIGURE 23. Enlargement of the $s \in [67.152, 67.16]$ interval of the top panel of figure 18. The instability threshold $e^{\lambda_r} = 1$ is indicated by a thin horizontal line and the saddle node corresponds to the change of stability indicated by the black circle.

collides on the positive real axis and splits. The state thus becomes (3, 2) unstable. Overall, the passage through this saddle node (and its vicinity) has added two unstable eigenvalues to the L_1^- state and it remains (3, 2) unstable along most of the subsequent negative segment. The branch then gains two more unstable eigendirections which collide with the previous two around the left fold, where the solution becomes (1, 4) unstable and the process then repeats.

From the previous discussion, it follows that all the secondary localized states are unstable and become more so as the structure broadens. The most unstable eigenmodes along the positive segments of the L_1^+ and L_1^- branches correspond to oscillatory instabilities arising after eigenvalue collisions (see figure 18) with growth rate in the vicinity of $e^{\lambda_r} = 1.2$. As shown in figure 20, the magnitude of the corresponding imaginary part of the complex eigenvalues reaches a maximum at each right fold, and then decreases towards the next left fold. Importantly, as we go up the snake, the number of unstable complex conjugate eigenvalues increases while their real parts remain comparable, and so do their imaginary parts. The presence of these eigenvalues is typical of non-gradient systems (Burke & Dawes 2012) and implies the emergence of non-trivial oscillatory dynamics in the vicinity of the corresponding fixed points. In contrast, the leading eigenvalues are real along most of the negative segments of the snake. Figure 24 summarizes all the unstable eigenmodes associated with an L_1^+ convecton computed at $Ra \approx 780.7143$ along the first negative segment of the branch as it begins snaking (see figure 24*a*). The oscillatory instability corresponding to panels (*b*) and (*c*) has complex growth rate $0.1485 \pm 0.5400i$ and, if triggered, is responsible for oscillatory tilt of the central roll about the vertical. This oscillatory instability is inherited from the eigenvalue collision right after the bifurcation of the L_1^+ state from the L^+ state but does not dominate along most of the negative branch segment. The dominant modes are instead the eigenmodes shown in (*d*) and (*e*), with real growth rates 0.2861 and 0.2860, respectively. The former leads to solutions with no remaining reflection symmetry and is akin to the eigenmode represented in figure 11(*c*): this mode creates a bifurcation to drifting rung states close to each fold. The latter is the amplitude mode that changes stability at the fold. Lastly, the odd parity drift mode in panel (*f*) is once again close to marginal (its growth rate is 7.715×10^{-4}). Thus, the growth of the rolls is observed first and is then followed by their rotation about the x axis. To understand the stability

https://doi.org/10.1017/jfm.2017.905 Published online by Cambridge University Press

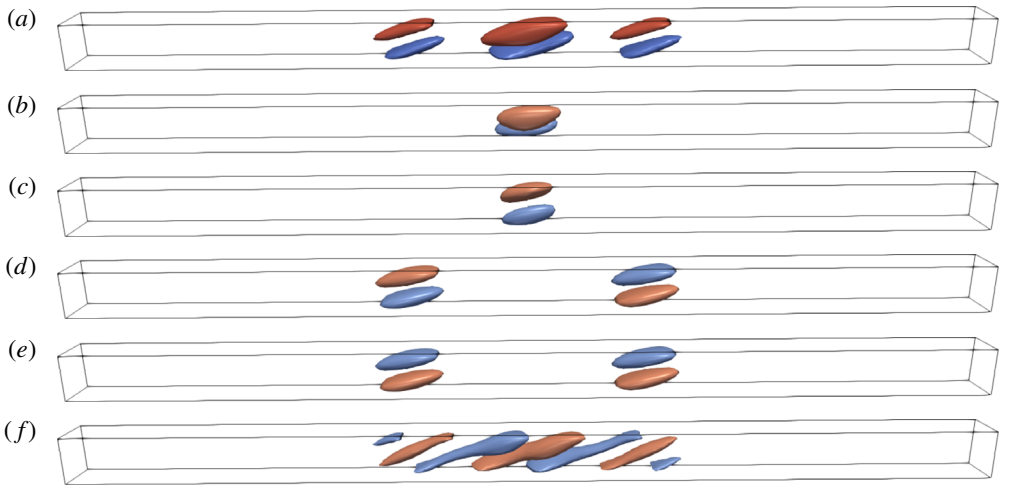


FIGURE 24. (Colour online) (*a*) L_1^+ convecton at $Ra \approx 780.7143$ ($s \approx 105$) on the first negative segment represented using the same colour scheme as in figure 3. All unstable eigenmodes are represented as in figure 9(*b*): panels (*b*) and (*c*) show the real and imaginary parts of the complex conjugate modes, while (*d*) and (*e*) show the new steady eigenmodes and (*f*) the odd parity drift mode.

changes along the secondary snaking branches, we represent in figure 25 all the unstable eigenmodes of a L_1^+ convecton at $Ra \approx 779.7672$ corresponding to the next positive branch segment. All three rolls are now of approximately the same strength (compare figure 25*a* to figure 24*a*) and the convecton is now 7 times unstable as opposed to being 5 times unstable as in figure 24(*a*). The mode responsible for the oscillations of the central roll is still unstable with growth rate $0.1379 + 0.5579i$. Two new unstable eigenmodes have appeared and undergone collisions with those shown in figure 24(*d*,*e*). These modes are shown next to those they are coupled to: the eigenmodes in figure 25(*d*,*e*) have growth rate $0.1605 \pm 0.4970i$ and are responsible for in-phase oscillations of the axes of the outer rolls of the convecton with respect to the y direction, while those in figure 25(*f*,*g*) have growth rate $0.1571 \pm 0.4959i$ and generate out-of-phase oscillations on the part of the outer rolls. Lastly, the odd parity drift mode is still present with the same small growth rate of 1.067×10^{-3} (figure 25*h*).

The process by which the stability properties evolve during the secondary snaking scenario repeats after each back and forth oscillation and each time is responsible for the addition of two pairs of unstable complex conjugate eigenvalues to the convecton spectrum. The evolution described here repeats for all subsequent branches of secondary states (not shown) with one main difference – the number of unstable eigenvalues inherited from the primary convecton branch: $L_{2\Delta}^+$ and L_{2c}^+ convectons are (6, 0) unstable before a double eigenvalue collision making them (2, 2) unstable while $L_{2\Delta}^-$ and L_{2c}^- convectons are originally (7, 0) unstable and turn into a (3, 2) unstable state. Moreover, since the new rolls are smaller than those on the primary convecton branches, it follows that the secondary snaking proceeds further than the primary snaking for given length of structure, implying that the twisted states can be more unstable than the primary states.

https://doi.org/10.1017/jfm.2017.905 Published online by Cambridge University Press

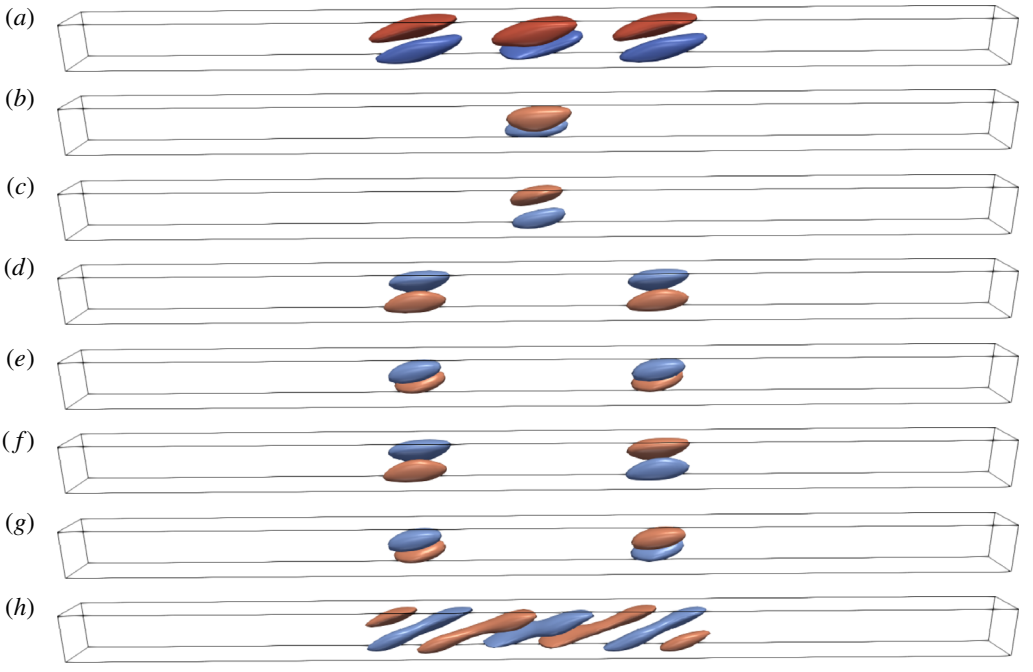


FIGURE 25. (Colour online) (*a*) L_1^+ convecton at $Ra \approx 779.7672$ ($s \approx 174$) on the second positive segment represented using the same colour scheme as in figure 3. All unstable eigenmodes are represented as in figure 9(*b*): panels (*b*) and (*c*) show the real and imaginary parts of the complex conjugate modes associated with the first eigenvalue collision (matching figure 24*b*,*c*), while panels (*d*) and (*e*), and (*f*) and (*g*), show the real and imaginary parts of the newly formed complex conjugate modes; (*h*) is the odd parity drift mode.

3.3. *Depinning*

The main differences between the two-dimensional system studied by Bergeon & Knobloch (2008*b*) and the three-dimensional system under investigation here can be understood in terms of the additional S_y symmetry. This symmetry gives rise to twist instabilities that are absent in the two-dimensional problem and these instabilities are in turn responsible for the emergence of secondary convectons. Moreover, it also impacts the dynamics outside the snaking region. In a typical depinning scenario, the convecton length grows in time via successive nucleation of additional rolls on either side of the structure. These nucleation events are interspersed with intervals of stasis during which the structure is almost steady. The time spent in the latter state grows with decreasing distance from the edge of the pinning region and does so as the inverse square root of the distance (Burke & Knobloch 2006) but this relationship has not been tested in fluid systems.

Figure 26 shows the dynamics at $Ra = 808$ of a convecton just outside the pinning region. The simulation was initialized using a convecton at the lower right saddle node on the L^+ branch ($Ra \approx 805.2252$) and run with and without imposing the symmetry S_y. The figure highlights the fundamental differences between S_y-symmetric dynamics and unconstrained direct numerical simulation (DNS). The symmetric dynamics behaves like the simulations reported by Bergeon & Knobloch (2008*b*): the front depins and rolls are sequentially added to both sides of the convecton until the

https://doi.org/10.1017/jfm.2017.905 Published online by Cambridge University Press

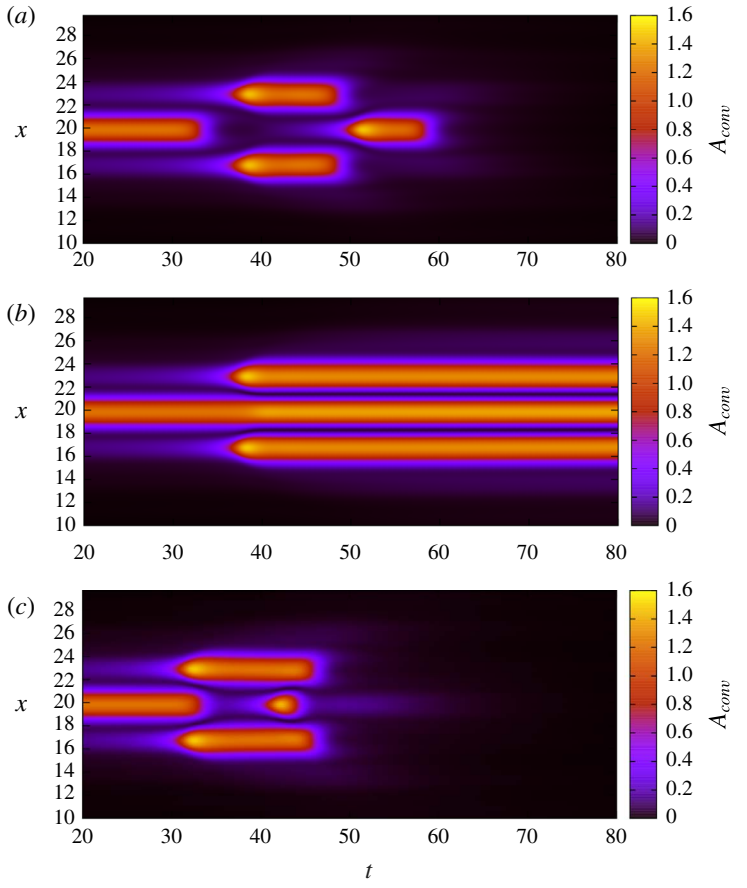


FIGURE 26. (Colour online) Space–time dynamics at $Ra = 808$ initialized with an L^+ convecton at the lower right fold corresponding to $Ra \approx 805.2252$ with no imposed symmetry (a) and with S_y symmetry imposed (b), and at $Ra = 809$ with no imposed symmetry (c). The solution is represented in the same way as in figure 17.

roll pattern fills the domain. This is not the case in the unconstrained DNS where the pattern decays to the conduction state when t reaches $t \approx 60$, as also found by Bergeon & Knobloch (2008*b*). The decay time in fact depends quite sensitively on the state used to initialize the simulation and does not vary monotonically with increasing Ra. For example, at $Ra = 807$, it takes 40 units of time to decay and no nucleation takes place (not shown but see figure 28*a* for a similar situation). At $Ra = 808$, it takes 60 units of time to decay but there are 'some' nucleation events, see figure 26(*a*). At $Ra = 809$ (figure 26*c*), it takes approximately 50 units of time: the nucleation event observed at $t = 35$ for $Ra = 808$ now occurs at $t = 30$ and the nucleated rolls survive until $t \approx 48$ (a similar time to $Ra = 808$) but the central roll reappears at $t = 40$ only to vanish at $t = 45$, whereas it only appeared at $t = 50$ for $Ra = 808$. Another fundamental difference concerns the behaviour of the central roll: this roll remains essentially unchanged in the symmetric simulation while it tilts and then decays between $t = 30$ and $t = 35$ in the DNS before temporarily regrowing. Despite this novel behaviour nucleation of new rolls still takes place and does so on a similar time scale as in the symmetric simulation. However, the DNS state at

https://doi.org/10.1017/jfm.2017.905 Published online by Cambridge University Press

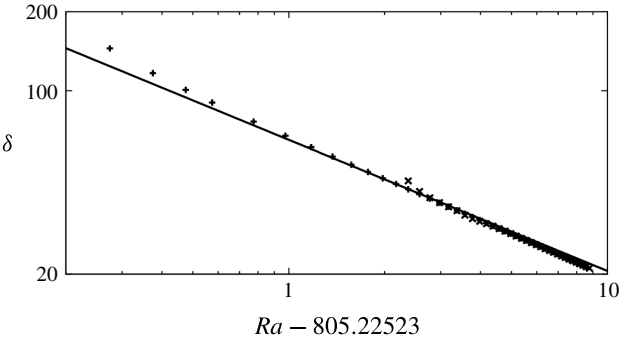


FIGURE 27. Time δ at which the first nucleation event occurs as a function of the Rayleigh number Ra for direct numerical simulations ('$\times$' signs) and for simulations with the symmetry S_y imposed ('+' signs). The straight line corresponds to the relation $\delta = 65(Ra - 805.22523)^{-0.5}$ expected on the basis of general theory.

$t = 40$ takes the form of two rolls separated by a roll-wide gap as opposed to a three-roll pattern in the symmetric simulation. The reappearance in the DNS of the central roll at $t \approx 50$ coincides with the decay of the two previously nucleated rolls. In each case, the decay of a roll is preceded by rotation of its axis suggesting that the decay is due to increased dissipation arising from the resulting closer approach to the adiabatic walls. Both simulations reveal a characteristic overshoot when a roll is nucleated, a property indicative of a non-gradient system and observed by Bergeon & Knobloch (2008*b*).

To compare the dynamics of our DNS to established depinning dynamics, we report in figure 27 the time at which the first nucleation event occurs in simulations initialized by the same solution as in figure 26. The figure shows a relatively good agreement between the inverse square root law found in other systems (Knobloch 2015) and the simulations with the symmetry S_y imposed. This agreement indicates that the two-dimensional system of Bergeon & Knobloch (2008*b*) behaves in a similar fashion to the Swift–Hohenberg equation (Burke & Knobloch 2006). On the other hand, the DNS provides substantially different results. Sufficiently far away from the fold, we recover the inverse square root law. However, for $Ra < 807.6$, this law breaks down and no depinning event is observed. The reason for this failure is that with no imposed symmetry, all the computed convecton states are unstable with respect to the twist instability and in the vicinity of a fold the time scale involved in the depinning process is so long that this instability kicks in before any nucleation can occur. A precursor to this behaviour can be seen in figure 26(*a*) where the central roll dies shortly after undergoing a rotation about the x axis, and does so at the same time as the nucleation of a pair of side rolls is taking place. For comparison, at $Ra = 807.6$ (not shown), the central roll decays on a similar time scale but the nucleation of the side rolls takes much longer, up to 45 units of time. If the Rayleigh number is decreased below 807.6, the central roll decays even further and there is no seed left for nucleation (see figure 28*a* for $Ra = 806$). Further away from the snaking interval, nucleation occurs much more quickly than twist and several nucleation events can be observed before any of the rolls decay, as exemplified in figure 28(*b*) for $Ra = 834$.

It remains to consider what happens when the Rayleigh number Ra moves past $Ra \approx 850.78$, the location of the primary pitchfork bifurcation. For $Ra \lesssim 850.78$ all solutions, as far as we can tell, decay to the stable conduction state. This is no longer possible once $Ra \gtrsim 850.78$ since the primary state is now unstable. In this regime (figure 29)

https://doi.org/10.1017/jfm.2017.905 Published online by Cambridge University Press

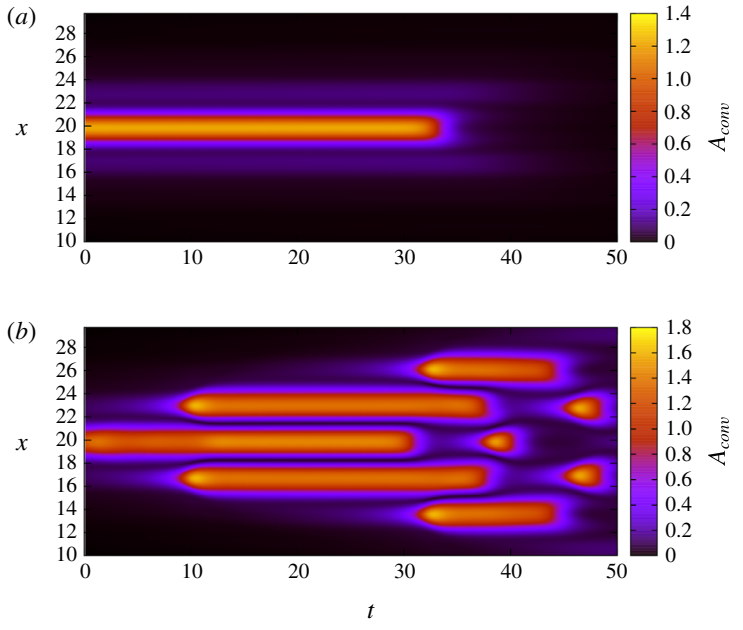


FIGURE 28. (Colour online) Space–time dynamics at (*a*) $Ra = 806$ and (*b*) $Ra = 834$ initialized with an L^+ convecton at the lower right fold corresponding to $Ra \approx 805.2252$ with no imposed symmetry. The solution is represented in the same way as in figure 17.

we find that the system exhibits relaxation oscillations resembling bursts. The figure shows that the flow frequently collapses towards the conduction state but does so in a spatially incoherent manner. As a result the rolls never completely disappear, and since the conduction state is now weakly unstable, they eventually grow back. As revealed in the figure both the collapse and the regrowth proceed by front propagation with well-defined speeds whereby the conduction state invades the roll state and *vice versa*. Moreover, because the collapse is spatially incoherent this behaviour results in irregular oscillations of relaxation type. Evidently this behaviour is a consequence of the competition between roll decay as a result of the twist instability and the linear instability of the conduction state acting as a regrowth mechanism, mediated via back-and-forth front propagation that maintains spatial asymmetry at all times, thereby guaranteeing spatially incoherent collapse and regrowth. The length of time the system spends near the conduction state depends on the initial condition prior to the initiation of the collapse event. Figure 29 shows episodes when the domain is almost devoid of convection ($t \approx 40$ and $t \approx 175$) as well as others when it is populated by a single roll ($t \approx 60$ and $t \approx 95$). Indeed figure 29(*a*) reveals the presence of a kind of 'quantization' reflecting the presence of $0, 1, 2, \ldots$ rolls in the domain with abrupt and irregular transitions between these states. Despite these types of regularity the final state represents spatio-temporal chaos since rolls may regrow at random locations owing to the instability of the background state. Figure 29(*b*) shows the appearance at $t \approx 190$ of an isolated roll near $x = 18$.

The situation resembles the behaviour of binary fluid convection in a horizontal layer just prior to the appearance of stable stationary convectons (Batiste *et al.* 2006) where it is a focusing instability that leads to intermittent dynamics from which the stationary convectons emerge.

https://doi.org/10.1017/jfm.2017.905 Published online by Cambridge University Press

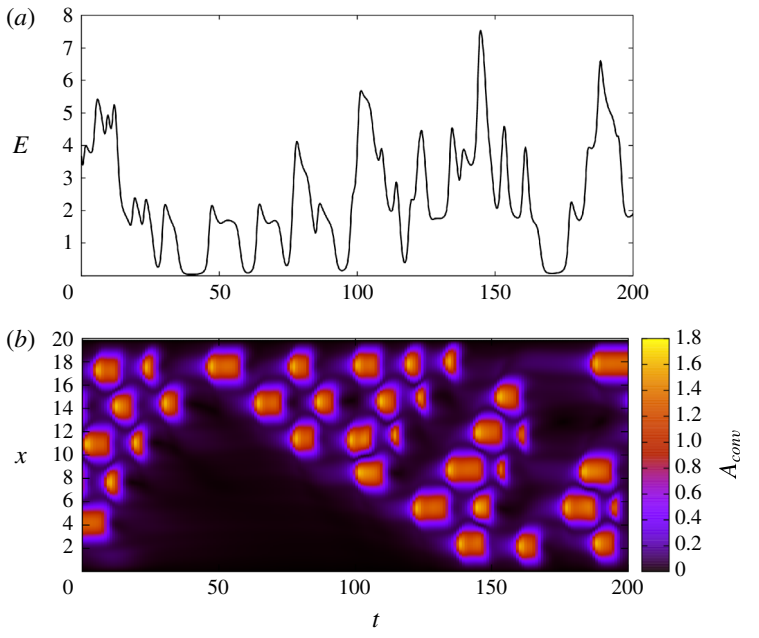


FIGURE 29. (Colour online) Relaxation oscillations observed at $Ra = 850.80$, in the vicinity of the primary instability ($Ra \approx 850.78$), shown through the temporal evolution of the kinetic energy (a) and through the corresponding space–time plot (b). The origin of time is chosen to fit the beginning of the visualized time frame.

4. Discussion

In this paper, we have discussed the stability of steady spatially localized doubly diffusive convection in a closed three-dimensional vertically extended cavity. These states, referred to as convectons, consist of an array of corotating rolls embedded in a background conduction state. Such a conduction state is only present when the contributions of the temperature and concentration to the buoyancy force balance, a key assumption made here in order to compare the present work with earlier work on the two-dimensional case with periodic boundary conditions in the vertical (Bergeon & Knobloch 2008*b*).

The domain studied is of long spatial extent in the vertical direction and of square cross-section in the horizontal. Convection is driven by temperature and concentration differences imposed on a pair of opposite vertical walls resulting in horizontal forcing, in contrast to the more common situation in which doubly diffusive convection takes place in a horizontal layer, driven by imposed temperature and concentration differences in the vertical. The latter geometry has been studied extensively in the context of binary fluid convection in the presence of a Soret effect (Batiste *et al.* 2006; Mercader *et al.* 2011) and exhibits behaviour that is quite close to that familiar from simple models of localized states such as the bistable Swift–Hohenberg equation (Burke & Knobloch 2006, 2007*b*). The present, vertically extended geometry is therefore of additional interest, both in order to understand the consequences of horizontal rather than vertical forcing, and also to elucidate the role played by the different symmetries of the system. Of these the symmetry S_Δ plays a prominent role (Bergeon & Knobloch 2008*b*) but in the present, three-dimensional case the transverse reflection S_y has dramatic consequences also.

https://doi.org/10.1017/jfm.2017.905 Published online by Cambridge University Press

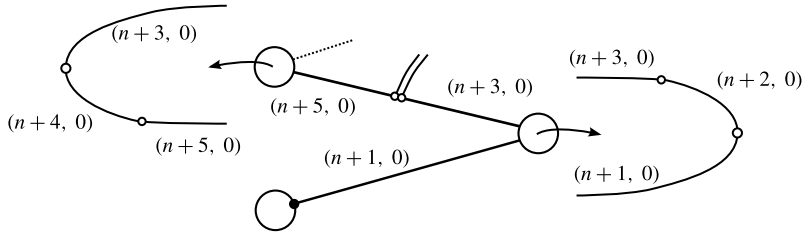


FIGURE 30. Scenario representing the stability of convectons $L^{\pm}$ along the primary snaking branches. Open circles represent bifurcations (either saddle nodes or pitchforks) while the filled circle represents an n-roll convecton based on which the scenario is proposed.

Since we impose no-slip boundary conditions on all the walls periodic structures are absent. In this case, as in other examples of this type (Mercader *et al.* 2009), a pair of convecton states bifurcates directly from the conduction state and after an interval of snaking ($703 < Ra < 807$) each evolves continuously with increasing Rayleigh number into a three-dimensional spatially extended domain-filling state. Twist instabilities that break the symmetry S_y of the primary snaking states are observed along the snaking branches and yield secondary twisted convectons whose branches display secondary snaking. These states are hybrid states: their core reflects the structure of the primary convecton from which they bifurcate while the side rolls generated via secondary snaking are typically weaker and have a different and smaller size, as well as being rotated about the x direction. Unfortunately, as shown here, the presence of the symmetry S_y leads to progressive destabilization of the localized states as one proceeds up both the primary snaking branches and the secondary snaking branches. Since these turn continuously into domain-filling states it follows that even domain-filling states are destabilized by the twist instability, a fact confirmed here by direct numerical simulation of the governing equations (cf. figure 5). In other words, our stability calculations confirm the numerical observation in Beaume *et al.* (2013*a*) that in the subcritical region below the primary pitchfork bifurcation all non-trivial states collapse to the stable conduction state and hence explain the absence of hysteresis at $Ra \approx 850.78$ observed in the transition from the subcritical regime to the finite-amplitude relaxation oscillations present beyond.

Except for the peculiarities due to the finite size of the domain or the choice of boundary conditions, the stability of a primary convecton can be predicted from the number of rolls within it, at least until the convectons start filling the domain. Figure 30 presents a scenario that is consistent with all our observations. To understand this scenario, let us consider a left saddle-node solution composed of an untwisted structure of n large rolls. Above the saddle node, on the positive branch segment, the solution is $(n+1, 0)$ times unstable, including the unstable eigenmodes corresponding to the tilt of each of the rolls (or combinations) as well as the odd parity drift eigenmode. This stability assignment remains unchanged until the subsequent saddle node on the right. At the right saddle node, the amplitude mode responsible for the nucleation of one new roll on either side of the pattern becomes unstable and the solution is then $(n + 2, 0)$ unstable. Soon thereafter, a phase eigenmode becomes unstable; this mode is responsible for the creation of rung states (it is a parity-breaking mode that usually results in drifting asymmetric states but here it results in asymmetric states attached to either the top or bottom domain boundary)

https://doi.org/10.1017/jfm.2017.905 Published online by Cambridge University Press

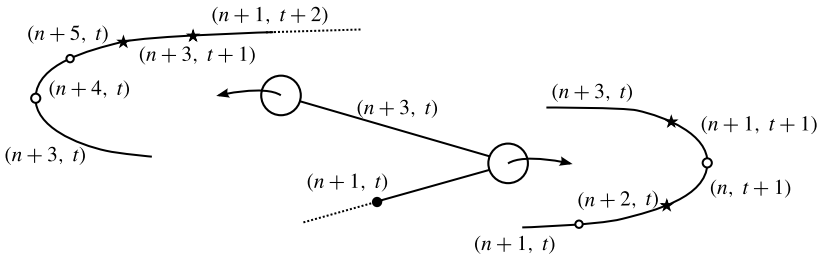


FIGURE 31. Same as figure 30 but for twisted convectons along the secondary snaking branch. The state represented by the filled circle consists of n large rolls and t small, twistable rolls. Stars represent eigenvalue collisions.

and the solution becomes $(n + 3, 0)$ unstable. On the negative branch segment that follows the stability of the state changes owing to a pair of nearby bifurcations generating twisted states: one eigenmode generates identical tilts in the two new rolls that start to emerge as one passes the right fold, while the other creates opposing tilts. After these two bifurcations, the state is $(n+5, 0)$ unstable and remains so until the phase eigenmode regains stability in the vicinity of the subsequent left saddle node, making the solution $(n+4, 0)$ unstable. At the saddle node the amplitude mode restabilizes, and the solution becomes $(n + 3, 0)$ times unstable. Since the number of rolls comprising the structure is $n+2$ this fact provides a simple rule for determining the number of unstable modes of a given convecton. This process persists for as long as the snaking continues. When the domain starts becoming full the branch L^+ turns towards larger Ra and no new bifurcations occur. The leading eigenvalues then evolve monotonically with Ra. For L^- the evolution is more complex and the state becomes more and more unstable, even after snaking terminates. Crucially, once the domain is full, the solution starts losing rolls in the centre and develops into a 2-pulse state that extends beyond the threshold for the primary instability ($Ra \approx 850$). These states are more unstable than the 1-pulse convectons discussed here.

For the twisted convectons a similar scenario applies and consists of two steps: the emergence of the branch of twisted states followed by repeated back and forth oscillations associated with secondary snaking. The scenario is summarized in figure 31. Near the secondary twist bifurcation, the branch of twisted convectons is $(n + 5, 0)$ times unstable. The unstable eigendirections correspond to the twist eigenmodes of the n large rolls and of the two small rolls surrounding them, together with the amplitude mode responsible for the creation of the small rolls, the phase mode associated with the near saddle-node bifurcations of the rung states in figure 30 and the odd parity drift eigenmode. Almost immediately the eigenvalues associated with the instabilities of the small rolls collide two by two. The first collision involves the eigenvalues associated with the amplitude eigenmode (responsible for the nucleation of the rolls) and the eigenmode responsible for the same sense rotation of the small rolls. The second collision involves the eigenvalues related to the phase eigenmode (a priori responsible for the rung states) and the eigenmode responsible for opposite sense rotation of the small rolls. After these two collisions, the stability of the twisted convecton is $(n + 1, 2)$. To continue describing the stability of these states, we need to introduce the number t of small rolls whose axes rotate about the vertical axis and consider a left saddle-node state consisting of n large unrotated rolls and t small rotated rolls. At a small distance beyond the saddle node, the stability is $(n + 1, t)$ and remains so until the vicinity of the

https://doi.org/10.1017/jfm.2017.905 Published online by Cambridge University Press

right saddle node. The unstable eigenmodes are the twist eigenmodes of the n large rolls, the odd parity drift mode and the eigenmodes associated with the t pairs of complex conjugate eigenvalues. The latter eigenmodes are responsible for oscillatory instabilities that produce un/rotation and growth/decay of the t small rolls. Close to the right saddle node, the twisted convecton undergoes a number of stability changes. Firstly, a phase eigenmode similar to those creating rung states becomes unstable and the convecton becomes $(n+2, t)$ unstable prior to the saddle node (cf. Burke & Dawes 2012). Shortly after, the eigenvalue associated with this eigenmode collides with that of the odd parity drift eigenmode to form a short-lived pair of complex conjugate eigenvalues. The convecton stability changes from $(n, t+1)$ to $(n+1, t+1)$ as it picks up another unstable eigendirection at the saddle node. This eigendirection is generated by an amplitude eigenmode responsible for the nucleation of side rolls. Very shortly after the saddle node, the odd parity drift and phase eigenmodes separate and the convecton is then $(n+3, t)$ unstable. At this stage, the unstable eigenmodes are the twist eigenmodes of the n large rolls, the odd parity drift mode, the amplitude and phase modes associated with the nucleation of small rolls and the t pairs of eigenmodes acting on the t small rolls by modifying their inclination and amplitude. The stability remains the same along the negative segment of the branch until the left saddle node where another amplitude eigenmode, resembling the first one, becomes unstable, followed by another phase eigenmode similar to that already unstable. After these two bifurcations, the convecton stability is $(n+5, t)$ and the two newly unstable eigenvalues collide almost immediately with the two coming from the previous saddle node. The first eigenvalue collision is that of the two amplitude modes, followed by that of the two phase eigenmodes. After these two eigenvalue collisions, the eigenmodes take on different roles: one acts on the roll tilt and the other on the amplitude, see figure 25. The stability of the convecton is $(n+1, t+2)$ and the process then repeats.

The above scenario breaks down for the first twist bifurcation along L^+ that yields a solution consisting of only one rotated small roll, without the accompanying second bifurcation. With this proviso the scenario is a reliable predictor of the convecton stability. In the case of periodic boundary conditions in x, the unstable odd parity drift eigenmode becomes marginal and serves as the generator of infinitesimal translations in the x direction. The primary convecton then has one fewer unstable eigendirection. Unfortunately, the stability of the twisted convectons does not follow so simply owing to the collisions between the drift and phase eigenvalues in the vicinity of the right saddle nodes.

We have seen that the spatio-temporal chaos identified here is a consequence of the simultaneous absence of stable stationary finite-amplitude states, be they spatially extended or localized, and the instability of the conduction state to which the system attempts to collapse when such states are unavailable. In small domains this mechanism is responsible for periodic relaxation oscillations. As explained in Bergeon & Knobloch (2002) these are present because the finite-amplitude state is unstable to a symmetry-breaking mode, and it is this mode that returns the system to the vicinity of the conduction state before the growth of a symmetric state takes the system back to the finite-amplitude state. In large domains this mechanism operates locally in space but does not occur coherently across the cell. This is a consequence of the fact that the asymmetric state now invades the conduction state via an asymmetric invasion front. Likewise the collapse phase of the oscillation also takes place via a front, this time with the conduction state displacing convection. Viewed this way it becomes apparent that the mechanism behind the incoherent relaxation oscillations observed in natural doubly diffusive convection is qualitatively

https://doi.org/10.1017/jfm.2017.905 Published online by Cambridge University Press

identical to that described by Nishiura & Ueyama (2001) for the Gray–Scott model, following earlier work on this system by Merkin *et al.* (1996*a*,*b*). In this system also the homogeneous state is unstable to a growing symmetric Turing mode, but the expected periodic state is itself unstable to a modulational instability that generates pulses that lead to the collapse of the periodic state and local return to the unstable homogeneous state. As in the Gray–Scott system the parameter regime where such incoherent relaxation oscillations are present is bounded from below by a simple bifurcation, the primary (subcritical) pitchfork at $Ra \approx 850.78$. However, in our system there appears to be no specific upper end: as Ra increases the growth of the unstable modes of the conduction state accelerates and the domain becomes filled with cells at all times. Front propagation is no longer observed except that every now and then a roll rotates and collapses. Thus spatio-temporal chaos persists to values of Ra in excess of $Ra = 900$. In contrast, in the Gray–Scott model the lower end of the interval of relaxation oscillations is determined by a (subcritical) Hopf bifurcation but there is an upper end as well, determined by a fold of the spatially periodic state. In both systems this type of large-amplitude dynamics sets in only when the domain is sufficiently large. Our work shows that this mechanism operates equally well in three-dimensional flows in bounded domains with realistic boundary conditions imposed on the boundaries, provided only that the domain is sufficiently extended in one direction, and therefore that it is robust. Indeed, a similar mechanism also operates in horizontally extended domains where it is a focusing instability that is responsible for the spatial inhomogeneity that is key to its operation (Batiste *et al.* 2006).

The results obtained in this paper follow a large scale numerical simulation effort to understand the dynamical implications of three-dimensionality on the stability of spatially localized states in fluids. The results have revealed clear shortcomings of the intuition developed on the basis of lower-dimensional systems (Knobloch 2015) and revealed a number of new phenomena, including secondary snaking, three-dimensional destabilization of all stationary states in the subcritical regime, and the abrupt transition to complex relaxation oscillations associated with the loss of stability of the background homogeneous state. A scenario has been formulated to simplify and extrapolate the linear stability results obtained here to other systems. These are expected to be helpful in other systems in which localized solutions are subject to three-dimensional instabilities such as plane Couette flow (Gibson & Schneider 2016) and two-component convection (Mercader, Alonso & Batiste 2008; Beaume *et al.* 2013*a*; Beaume, Knobloch & Bergeon 2013*b*; Watanabe *et al.* 2016) and suggest that spatially incoherent relaxation oscillations are a general feature of this class of spatially extended systems.

Acknowledgements

One of us (E.K.) would like to thank Professor Y. Nishiura for bringing his 2001 paper to his attention. Some of this work was undertaken on ARC2, part of the High Performance Computing facilities at the University of Leeds, UK. Partial support from the National Science Foundation under grant DMS-1613132 (E.K.) is gratefully acknowledged.

REFERENCES

AVILA, M., MELLIBOVSKY, F., ROLAND, N. & HOF, B. 2013 Streamwise-localized solutions at the onset of turbulence in pipe flow. *Phys. Rev. Lett.* **110**, 224502.

https://doi.org/10.1017/jfm.2017.905 Published online by Cambridge University Press

AVITABILE, D., LLOYD, D. J. B., BURKE, J., KNOBLOCH, E. & SANDSTEDE, B. 2010 To snake or not to snake in the planar Swift–Hohenberg equation. *SIAM J. Appl. Dyn. Syst.* **9**, 704–733.

BATISTE, O., KNOBLOCH, E., ALONSO, A. & MERCADER, I. 2006 Spatially localized binary-fluid convection. *J. Fluid Mech.* **560**, 149–158.

BEAUME, C. 2017 Adaptive Stokes preconditioning for steady incompressible flows. *Commun. Comput. Phys.* **22**, 494–516.

BEAUME, C., BERGEON, A. & KNOBLOCH, E. 2011 Homoclinic snaking of localized states in doubly diffusive convection. *Phys. Fluids* **23**, 094102.

BEAUME, C., BERGEON, A. & KNOBLOCH, E. 2013*a* Convectons and secondary snaking in three-dimensional natural doubly diffusive convection. *Phys. Fluids* **25**, 024105.

BEAUME, C., KNOBLOCH, E. & BERGEON, A. 2013*b* Nonsnaking doubly diffusive convectons and the twist instability. *Phys. Fluids* **25**, 114102.

BERGEON, A. & KNOBLOCH, E. 2002 Natural doubly diffusive convection in three-dimensional enclosures. *Phys. Fluids* **14**, 3233–3250.

BERGEON, A. & KNOBLOCH, E. 2008*a* Periodic and localized states in natural doubly diffusive convection. *Physica* D **237**, 1139–1150.

BERGEON, A. & KNOBLOCH, E. 2008*b* Spatially localized states in natural doubly diffusive convection. *Phys. Fluids* **20**, 034102.

BRAND, E. & GIBSON, J. F. 2014 A doubly localized equilibrium solution of plane Couette flow. *J. Fluid Mech.* **750**, R3.

BURKE, J. & DAWES, J. H. P. 2012 Localized states in an extended Swift–Hohenberg equation. *SIAM J. Appl. Dyn. Syst.* **11**, 261–284.

BURKE, J. & KNOBLOCH, E. 2006 Localized states in the generalized Swift–Hohenberg equation. *Phys. Rev.* E **73**, 056211.

BURKE, J. & KNOBLOCH, E. 2007*a* Homoclinic snaking: structure and stability. *Chaos* **17**, 037102.

BURKE, J. & KNOBLOCH, E. 2007*b* Snakes and ladders: localized states in the Swift–Hohenberg equation. *Phys. Lett.* A **360**, 681–688.

DANGELMAYR, G., HETTEL, J. & KNOBLOCH, E. 1997 Parity-breaking bifurcation in inhomogeneous systems. *Nonlinearity* **74**, 1093–1114.

DUGUET, Y., SCHLATTER, P. & HENNINGSON, D. 2009 Localized edge states in plane Couette flow. *Phys. Fluids* **21**, 111701.

GHORAYEB, K. & MOJTABI, A. 1997 Double diffusive convection in a vertical regular cavity. *Phys. Fluids* **9**, 2339–2348.

GIBSON, J. F. & BRAND, E. 2014 Spanwise-localized solutions of planar shear flows. *J. Fluid Mech.* **745**, 25–61.

GIBSON, J. F. & SCHNEIDER, T. M. 2016 Homoclinic snaking in plane Couette flows: bending, skewing and finite-size effects. *J. Fluid Mech.* **794**, 530–551.

HIRSCHBERG, P. & KNOBLOCH, E. 1997 Mode interactions in large aspect ratio convection. *J. Nonlinear Sci.* **7**, 537–556.

KAO, H.-C., BEAUME, C. & KNOBLOCH, E. 2014 Spatial localization in heterogeneous systems. *Phys. Rev.* E **89**, 012903.

KHAPKO, T., KREILOS, T., SCHLATTER, P., DUGUET, Y., ECKHARDT, B. & HENNINGSON, D. 2013 Localized edge states in the asymptotic suction boundary layer. *J. Fluid Mech.* **717**, R6.

KNOBLOCH, E. 2015 Spatial localization in dissipative systems. *Annu. Rev. Cond. Mat. Phys.* **6**, 325–359.

KNOBLOCH, E., HETTEL, J. & DANGELMAYR, G. 1995 Parity breaking bifurcation in inhomogeneous systems. *Phys. Rev. Lett.* **74**, 4839–4842.

LIOUBASHEVSKI, O., HAMIEL, Y., AGNON, A., RECHES, Z. & FINEBERG, J. 1999 Oscillons and propagating solitary waves in a vertically vibrated colloidal suspension. *Phys. Rev. Lett.* **83**, 3190–3193.

LLOYD, D. J. B., GOLLWITZER, C., REHBERG, I. & RICHTER, R. 2015 Homoclinic snaking near the surface instability of a polarizable fluid. *J. Fluid Mech.* **783**, 283–305.

LO JACONO, D., BERGEON, A. & KNOBLOCH, E. 2017 Localized traveling pulses in natural doubly diffusive convection. *Phys. Rev. Fluids* **2**, 093501.

https://doi.org/10.1017/jfm.2017.905 Published online by Cambridge University Press

MELLIBOVSKY, F. & MESEGUER, A. 2015 A mechanism for streamwise localisation of nonlinear waves in shear flows. *J. Fluid Mech.* **779**, R1.

MERCADER, I., ALONSO, A. & BATISTE, O. 2008 Spatiotemporal dynamics near the onset of convection for binary mixtures in cylindrical containers. *Phys. Rev.* E **77**, 036313.

MERCADER, I., BATISTE, O., ALONSO, A. & KNOBLOCH, E. 2009 Localized pinning states in closed containers: Homoclinic snaking without bistability. *Phys. Rev.* E **80**, 025201(R).

MERCADER, I., BATISTE, O., ALONSO, A. & KNOBLOCH, E. 2011 Convectons, anticonvectons and multiconvectons in binary fluid convection. *J. Fluid Mech.* **667**, 586–606.

MERCADER, I., BATISTE, O., ALONSO, A. & KNOBLOCH, E. 2013 Travelling convectons in binary fluid convection. *J. Fluid Mech.* **722**, 240–266.

MERKIN, J. H., PETROV, V., SCOTT, S. K. & SHOWALTER, K. 1996*a* Wave-induced chaos in a continuously fed unstirred reactor. *J. Chem. Soc. Faraday Trans.* **92**, 2911–2918.

MERKIN, J. H., PETROV, V., SCOTT, S. K. & SHOWALTER, K. 1996*b* Wave-induced chemical chaos. *Phys. Rev. Lett.* **76**, 546–549.

NISHIURA, Y. & UEYAMA, D. 2001 Spatio-temporal chaos for the Gray–Scott model. *Physica* D **150**, 137–162.

SCHNEIDER, T. M., GIBSON, J. F. & BURKE, J. 2010*a* Snakes and ladders: localized solutions of plane Couette flow. *Phys. Rev. Lett.* **104**, 104501.

SCHNEIDER, T. M., MARINC, D. & ECKHARDT, B. 2010*b* Localized edge states nucleate turbulence in extended plane Couette cells. *J. Fluid Mech.* **646**, 441–451.

SEZAI, I. & MOHAMAD, A. A. 2000 Double diffusive convection in a cubic enclosure with opposing temperature and concentration gradients. *Phys. Fluids* **12**, 2210–2223.

THANGAM, S., ZEBIB, A. & CHEN, C. F. 1982 Double-diffusive convection in an inclined fluid layer. *J. Fluid Mech.* **116**, 363–378.

WATANABE, T., IIMA, M. & NISHIURA, Y. 2012 Spontaneous formation of travelling localized structures and their asymptotic behaviour in binary fluid convection. *J. Fluid Mech.* **712**, 219–243.

WATANABE, T., IIMA, M. & NISHIURA, Y. 2016 A skeleton of collision dynamics: Hierarchical network structure among even-symmetric steady pulses in binary fluid convection. *SIAM J. Appl. Dyn. Syst.* **15**, 789–806.

WOODS, P. D. & CHAMPNEYS, A. R. 1999 Heteroclinic tangles and homoclinic snaking in the unfolding of a degenerate reversible Hamiltonian–Hopf bifurcation. *Physica* D **129**, 147–170.

XIN, S., LE QUÉRÉ, P. & TUCKERMAN, L. S. 1998 Bifurcation analysis of double-diffusive convection with opposing horizontal thermal and solutal gradients. *Phys. Fluids* **10**, 850–858.

https://doi.org/10.1017/jfm.2017.905 Published online by Cambridge University Press